

Electromagnetical model of an induction motor in COMSOL Multiphysics

VIKTOR WILOW



KTH Electrical Engineering

Degree project in
Electrical Engineering
Master of Science
Stockholm, Sweden 2014

XR-EE-E2C 2014:004



ROYAL INSTITUTE
OF TECHNOLOGY



Electromagnetical model of an induction motor in COMSOL Multiphysics

By

Viktor Wilow

Master Thesis

Supervisor:
Romain Haettel

Examiner:
Chandur Sadarangani

Royal Institute of Technology
School of Electrical Engineering
Electrical Energy Conversion

Stockholm 2014
XR-EE-E2C 2014:004

ABSTRACT

Ansys, Flux or COMSOL are examples of software-tools that can be used to study magnetic noise, caused by magnetic forces in the air-gap, in induction motors. The project team wanted to use COMSOL in this thesis. The electromagnetical domain needs to be coupled to the mechanical domain to complete the study. The air-gap forces, calculated in the electromagnetical model using the Rotating Machinery module, can be exported to the Acoustic-Solid Interaction module in COMSOL to enable the vibro-acoustic analysis.

An electromagnetical model of an induction motor is developed in two-dimensions in the finite element method based software-tool COMSOL Multiphysics in this thesis. Simulation results obtained in the frequency domain are compared with results achieved in the software-tool FEMM. Simulation results of the phase inductance, distribution of the flux density and the torque are compared. The simulated torque in COMSOL is validated with the torque derived based on an equivalent lumped model of the induction motor. A time-dependent simulation of the motor is made at 4.7% slip and 1A (peak) supply. The obtained torque is 0.33Nm. The same value is achieved in the frequency study in COMSOL. The corresponding value is 0.003Nm higher in FEMM. The evaluated air-gap forces at 4.7% slip can be used for studying vibro-acoustics in COMSOL.

Index terms: *Electromagnetical model, Induction motor, Finite element method, COMSOL Multiphysics.*

SAMMANFATTNING

Ansys, Flux eller COMSOL är exempel på datorprogram som kan användas för att studera magnetiskt brus, orsakad av magnetiska krafter i luftgapet, i induktionsmotorer. Projektgruppen ville använda COMSOL i det här examensarbetet. För att kunna utföra studien måste den elektromagnetiska domänen kopplas till den mekaniska domänen. Luftgapskrafterna, beräknade i den elektromagnetiska modellen genom att använda modulen för roterande maskiner, kan exporteras till modulen Acoustic-Solid Interaction för att möjliggöra den vibro-akustiska analysen.

En elektromagnetisk modell av en induktionsmotor är utvecklad i två dimensioner i finita elementmetoden-baserade programvaran COMSOL Multiphysics i det här examensarbetet. Simuleringsresultat från frekvensdomänen jämförs med resultat som uppnås med datorprogramvaran FEMM. Simuleringsresultat för fas-induktansen, fördelningen av flödestätheten och momentet jämförs. Det simulerade momentet i COMSOL valideras med momentet som härleds utifrån induktionsmotorns motsvarande ekvivalenta schema. En tidsberoende motor-simulering genomförs vid 4.7% slip, matad med 1A (topp-värde). Det erhållna momentet är 0.33Nm. Samma värde erhålls i frekvensstudien i COMSOL. Värdet är 0.003Nm högre i FEMM. De beräknade luftgapskrafterna vid 4.7% slip kan användas för att göra en vibro-akustisk studie i COMSOL.

Sökord: *Elektromagnetisk modell, Induktionsmotor, Finita elementmetoden, COMSOL Multiphysics.*



Master Thesis Report

Corporate Research & KTH



Doc. title

By: Viktor Wilow

Page

Electromagnetical model of an induction motor in COMSOL Multiphysics

iii/v

ACKNOWLEDGEMENT

This Master Thesis work was made in collaboration with Kungliga Tekniska Högskolan in Stockholm and ABB Corporate Research in Västerås. ABB has participated in financing this project.

I express my deepest gratitude to my examiner at KTH, Prof. Chandur Sadarangani and my supervisor at ABB, Dr. Romain Haettel. Special thanks to Tec. Lic. Rathna Chitroju at LV-motors for the meetings we had and for his support. Thanks to M.Sc. Mustafa Kavasoglu at ABB CRC.

This report is dedicated to my beloved family.

Viktor Wilow

Stockholm, 2014-03-26.

TABLE OF CONTENTS

	PAGE:
LIST OF SYMBOLS	1
GLOSSARY	2
CHAPTER 1 INTRODUCTION	3
1.1 NOISE IN INDUCTION MOTORS	3
1.2 SOFTWARE-TOOLS FOR STUDYING VIBRO-ACOUSTICS OF AN INDUCTION MOTOR.....	3
1.2.1 ANSYS.....	3
1.2.2 FLUX.....	4
1.2.3 COMSOL MULTIPHYSICS.....	4
1.3 PROBLEM DESCRIPTION.....	5
1.4 PREVIOUS ELECTROMAGNETICAL STUDIES OF INDUCTION MOTORS IN COMSOL.....	5
1.5 THESIS OBJECTIVES.....	6
1.6 METHOD.....	6
1.7 THESIS OUTLINE.....	7
CHAPTER 2 FEM-MODEL OF A SQUIRREL-CAGE INDUCTION MOTOR	8
2.1 PRINCIPLE OPERATION OF A SQUIRREL-CAGE INDUCTION MOTOR.....	8
2.2 ROTOR BAR TOPOLOGY	8
2.3 SINUSOIDAL VOLTAGE SUPPLY ON A THREE-PHASE WINDING ARRANGEMENT	9
2.4 CONNECTION OF THE STATOR WINDING PHASES	10
2.5 MAGNETIZATION CURVE	11
2.6 TRIANGULAR MESH IN A 2D PROBLEM FORMULATION.....	12
2.7 DIFFERENTIAL FORM OF MAXWELL'S EQUATIONS.....	12
2.8 MAGNETIC VECTOR POTENTIAL	13
2.9 STATOR FLUX LINKAGE.....	13
2.10 SKIN EFFECT.....	13
2.11 FORCE-CALCULATION	14
CHAPTER 3 LUMPED MODEL OF THE INDUCTION MOTOR	15
3.1 SIMPLIFIED ELECTRIC CIRCUIT.....	15
3.2 ELECTRIC-CIRCUIT BASED ANALYSIS.....	15
CHAPTER 4 FEM-MODEL OF THE IM IN COMSOL MULTIPHYSICS	18
4.1 DESCRIPTION OF THE STUDIED INDUCTION MOTOR.....	18
4.2 BOUNDARY CONDITIONS	19
4.3 MATERIAL	19
4.4 ELEMENT QUALITY OF THE MESH	19
4.5 AIR-GAP MESH DENSITY	20
4.6 SOLVED EQUATION.....	20
CHAPTER 5 TIME-HARMONIC SIMULATION OF THE INDUCTION MOTOR	21
5.1 STATOR FLUX LINKAGE IN PHASE A	21
5.2 DISTRIBUTION OF THE MAGNETIC FLUX DENSITY	22
5.3 POINT-EVALUATION OF THE MAGNETIC FLUX DENSITY.....	23
5.4 AIR-GAP FLUX DENSITY AT NO-LOAD	24
5.5 VALIDATION OF THE SIMULATED TORQUE	26
5.6 COMPARISON BETWEEN SIMULATED PHASE INDUCTANCE AND TORQUE.....	28



Master Thesis Report
Corporate Research & KTH



Doc. title

By: Viktor Wilow

Page

Electromagnetical model of an induction motor in COMSOL Multiphysics

v/v

CHAPTER 6	TIME-DEPENDENT SIMULATION OF THE IM IN COMSOL	30
6.1	STATOR- AND ROTOR- CURRENT	30
6.2	STATOR FLUX LINKAGE AND STATOR PHASE VOLTAGE	32
6.3	TORQUE AT 4.7% SLIP IN COMSOL MULTIPHYSICS	34
6.4	FLUX DENSITY ALONG THE MIDDLE OF THE AIR-GAP	35
6.5	AIR-GAP FORCE	36
CHAPTER 7	CONCLUSION AND FUTURE WORK	37
7.1	CONCLUSION	37
7.2	FUTURE WORK	37
BIBLIOGRAPHY		38
LIST OF FIGURES		40
LIST OF TABLES		41
APPENDIX A	SPECIFICATION OF THE INDUCTION MOTOR	I
APPENDIX B	STATOR SLOT FILL FACTOR	II

LIST OF SYMBOLS

Symbol:	Description:	Page:	Symbol:	Description:	Page:
q	Slots per pole per phase.....	9	A_z	Magnetic vector potential	13
τ_p	Pole-pitch	9	S	Surface	13
\hat{V}	Peak-value of the stator voltage	9	δ_{skin}	Skin depth	13
V_a	Voltage supply in phase A	9	ρ_{bar}	Rotor bar resistivity	13
ω	Angular speed	9	f	Frequency	13
t	Time	9	σ_r	Radial magnetic force.....	14
V_b	Stator voltage supply in phase B ...	9	B_n	Normal component of the flux density	14
V_c	Stator voltage supply in phase C .	10	B_t	Tangential component of the magnetic flux density.....	14
V_{ba}	Line-to-line voltage between phase B and A.....	10	σ_t	Tangential magnetic force	14
V_{ac}	Line-to-line voltage between phase A and C.....	10	V_s	Stator voltage supply.....	15
B	Magnetic flux density	11	i_s	Stator phase current.....	15
μ_r	Relative magnetic permeability	11	i_M	Magnetizing current.....	15
μ_0	Vacuum permeability	11	i_r	Rotor current	15
H	Magnetic field intensity	11	R_s	Stator resistance	15
B_r	Remanent magnetic flux density..	11	$L_{\lambda s}$	Stator leakage inductance	15
H_c	Coercive field strength.....	11	L_M	Mutual inductance	15
δ	Air-gap thickness.....	12	R_r	Rotor resistance	15
E	Electric field (vector form)	12	s	Slip.....	15
B	Magnetic flux density (vector form).....	12	ω_s	Angular speed of stator (mechanical)	15
H	Magnetic field intensity (vector form).....	12	ω_m	Angular speed of rotor (mechanical)	15
J	Current density (vector form).....	12	p_p	Number of pole pairs.....	15
D	Electric displacement field (vector form).....	12	ω_1	Angular speed of stator (electrical)	15
ρ	Electric charge density	12	ω_{slip}	Angular slip frequency.....	15
A	Magnetic vector potential (vector form).....	13	τ	Rotor time constant	15
e_z	Unit vector in the z-direction	13	Z_{phase}	Total phase impedance	16
ψ_s	Stator flux linkage (per phase).....	13	j	Imaginary unit	16
N_t	Number of turns per stator slot	13	L_{phase}	Phase inductance.....	16
A_{ss}	Stator slot area.....	13	L_r	Real part of the phase inductance	16
L	Lamination length	13	L_i	Imaginary part of the phase inductance.....	16
$+Q_s$	Stator slots with positive direction of the current density	13			
$-Q_s$	Stator slots with negative sign of the current density	13			

c_1	Values that minimize the error 16	\hat{B}_r	Maximum radial flux density (average value) 23
c_2	Values that minimize the error 16	\hat{B}_t	Maximum tangential flux density (average value) 23
P_δ	Air-gap power 16	$B_{\delta,rad}$	Radial flux density spanning over one pole-pitch around the middle of the air-gap 24
T_e	Electromagnetic torque..... 17	$B_{\delta,tang}$	Tangential flux density covering one pole-pitch in the middle of the air-gap..... 24
P_{mech}	Mechanical power 17	T_{avz}	Average valued torque 26
A_Δ	Area of a triangular element 19	n	Harmonic number..... 32
$l_{k,\Delta}$	Side-length k of a triangular element 19	F_{fys}	Stator slot fill factor..... II
q_Δ	Element quality for a triangle 19	A_{wire}	Wire area II
k	Index number 19		
σ	Electrical conductivity 20		
v	Velocity (vector form)..... 20		
ψ_{sa}	Stator flux linkage of phase A 21		

GLOSSARY

Glossary:	Description:	Page:
Ansys	The sub software-tools Ansys Maxwell, Ansys Mechanical and Ansys Acoustics Structures can be used for the vibro-acoustic study. The couplings are made in Ansys Workbench. The latest release of Ansys is, in the time of writing, version 15 3	3
Flux	FEM-based software-tool which is developed by CEDRAT. The latest version is, in the time of writing, release 11.2..... 3	3
COMSOL	Numerical software-tool based on FEM for making the electromagnetical model of the induction motor. COMSOL version 4.4, which is the latest release in the time of writing, is benchmarked with FEMM 3	3
PM	Permanent Magnet 3	3
2D	Two-dimensional..... 3	3
3D	Three-dimensional 3	3
MSC Nastran	Mechanical software-tool which is coupled to Flux in the indirect method to study vibro-acoustics of an induction motor 4	4
IM	Induction motor 5	5
DFMZS	Software-tool used for validating the COMSOL model in reference [10]..... 5	5
FEMM	Time-harmonic simulations are made in this FEM-based software tool to compare results obtained in COMSOL of the induction motor. 6	6
EM	Electromagnetic 6	6
FEM	Finite element method 8	8
AC	Alternating current 9	9
RMS	Root mean square 17	17
KCL	Kirchhoff's current law..... 17	17

CHAPTER 1 INTRODUCTION

1.1 NOISE IN INDUCTION MOTORS

The robust induction motors are electrical motors which are widely used in industrial applications, such as traction, compressors and pumps [1]. Electrical motors are designed to convert electrical energy to mechanical power at highest efficiency possible [2].

The transformation from electrical- to mechanical- energy, during motor operation also causes so called parasitic effects. Magnetic noise, incited from the radial air-gap forces, is an example of these unwanted effects. [3] Sources of noise in induction motors are, other than for the magnetic causes, generated from the bearings and the cooling system [2, 4]. *Section 1.2* describes the procedure of analyzing acoustic noise due to the air-gap forces caused by the electro-magnetic field in the air-gap.

There are restrictions to fulfill on the noise level in induction motors. Therefore, it is vital to predict these levels using appropriate tools to select a strategy for noise control. [4]

1.2 SOFTWARE-TOOLS FOR STUDYING VIBRO-ACOUSTICS OF AN INDUCTION MOTOR

Ansys, Flux or COMSOL Multiphysics are examples of software tools that can be used for the vibro-acoustic study of an induction motor. Analyzing magnetic noise in an induction motor requires multiphysical couplings. The electromagnetical domain is linked to the mechanical domain since the magnetic forces in the air-gap, created from the moving magnetic field, induce stator vibrations that produce the magnetic noise.

1.2.1 ANSYS

The American-developed software-tool Ansys is used in reference [5] to predict magnetic noise in a PM-motor. The one-way coupling procedure, used in reference [5], is seen in *Figure 1-1*. Reference [5] states that the process is not reversible since the noise does not stimulate the motor structure and the vibrations of the stator housing do not affect the electromagnetic field. The couplings between the sub software-tools Ansys Maxwell, Ansys Mechanical and Ansys Acoustics Structures are allocated and visualized in Ansys Workbench. A transient electromagnetic 2D-model is simulated at rated speed in Ansys Maxwell. The air-gap forces are calculated on the arc line using Maxwell's stress tensor. The equations of the radial- and tangential- force components are given in *Section 2.11*. The force vectors, one for each stator tooth, are transformed to the frequency domain and mapped to the nodes of a 3D mechanical mesh required for the vibratory analysis. A harmonic response analysis is conducted to study the vibration of the structure in Ansys Mechanical. The response amplitude is analyzed in the frequency domain to obtain resonance frequencies that cause acoustic noise. Resonance occurs if the natural frequency of the structure coincides with the frequency of the radial magnetic force [6]. The displacements are exported to Ansys Acoustics Structures where the acoustic analysis is made to evaluate the sound pressure level.

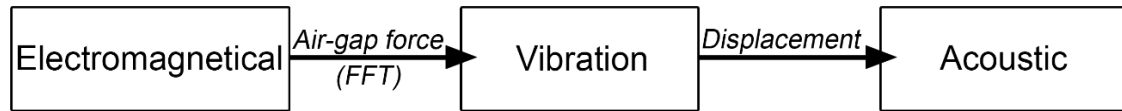


Figure 1-1 Coupling procedure for a vibro-acoustic analysis of an induction motor.

1.2.2 FLUX

It is described in references [7, 8] how the French software-tool Flux, which is developed by CEDRAT, can be used for the vibro-acoustic analysis. The transient electromagnetical model of the motor is simulated in Flux. The air-gap forces are computed along the circumference in the air-gap by using Maxwell's stress tensor. The indirect methodology for analyzing vibro-acoustics using Flux is illustrated in *Figure 1-2*. The method is indirect since the 3D mechanical mesh created in MSC Nastran is exported to the post-processing in Flux and exported to MSC Nastran together with the projected magnetic forces. The vibro-acoustic analysis is made in MSC Nastran.

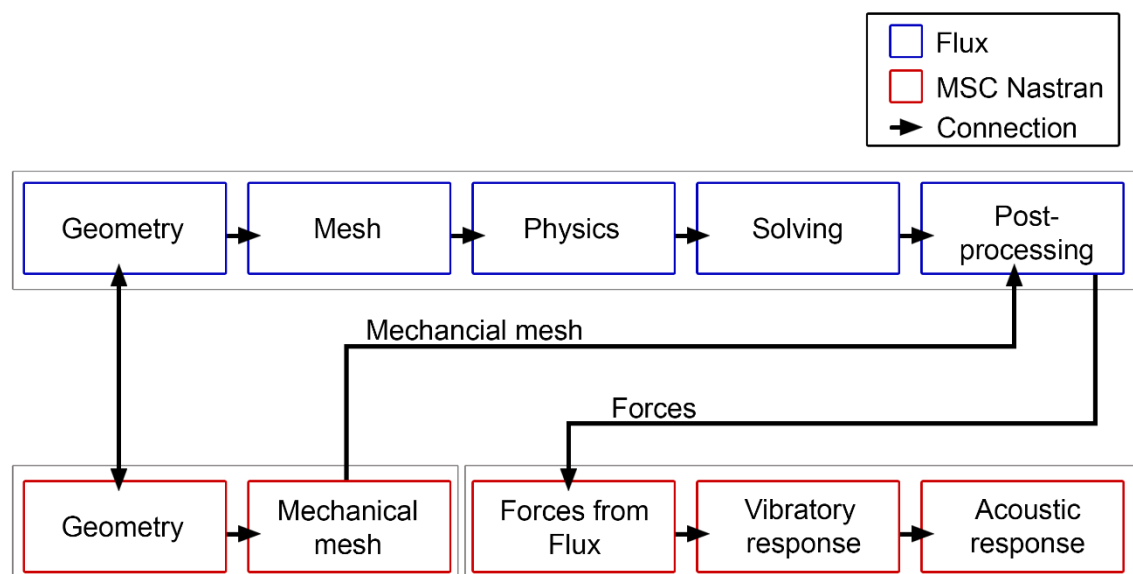


Figure 1-2 Indirect method for studying vibro-acoustics in Flux, [8].

1.2.3 COMSOL MULTIPHYSICS

The vibro-acoustic study can, according to the COMSOL Support Team, be made by coupling two modules directly in COMSOL Multiphysics. The transient electromagnetic model is simulated in the Rotating Machinery module. The magnetic forces, transformed to the frequency domain, can be inserted in the module for Acoustic-Solid Interaction. The vibratory study and the acoustic analysis are solved as a two-way coupling.

1.3 PROBLEM DESCRIPTION

The prerequisite of this work is to develop an electromagnetic model that can calculate the electromagnetic field and forces in an IM. The project team wanted to explore the limits and development of COMSOL Multiphysics.

1.4 PREVIOUS ELECTROMAGNETICAL STUDIES OF INDUCTION MOTORS IN COMSOL

This section is an overview of the COMSOL conference proceedings in references [9, 10]. *Table 1-1* and *Table 1-2* summarize the main differences and similarities in these articles.

Two pole squirrel-cage induction motors are simulated in COMSOL Multiphysics. A time-harmonic study is made in reference [9] to study the steady state performance of a double-cage rotor. Static simulations are made at different slip values. Reference [10] investigates the dynamic behavior of a single-cage rotor. Simulation results at standstill and at constant speed in COMSOL Multiphysics corresponds to results achieved in the software-tool DFMZS. The start-up is simulated based on the validated COMSOL model. One pole pitch, half of the geometry in this instance, of the 2D cross-section is modeled in references [9, 10]. Anti-periodic boundary conditions are applied on the intersected boundaries. Reference [9] assumes linear ferromagnetic materials instead of using an effective relative magnetic permeability. However, the ferromagnetic materials follow the magnetization curve in reference [10]. Thus, the magnetic permeability of the iron-core material is constant in reference [9] but could reach saturation in reference [10]. References [9, 10] state that it is important to use a proper mesh of the air-gap since it is a critical region. Modelling in two dimensions neglects the impact of the stator end-windings and rotor end-rings in the field model. These effects are included, in references [9, 10], through the coupling of external circuits to the field model. The coupling procedure is illustrated in *Figure 7-1*. References [9, 10] mention that the overhang effects are important to consider in the electromagnetic model as they influence the output results, such as torque. Reference [10] claims that it is possible to model the end-effects either by using the electric circuit interface or by typing in the circuit relations as differential equations in COMSOL Multiphysics. References [9, 10] state that it is essential to supply the stator with voltage instead of current. The reason is that current is an output parameter determined by the circuit equations in the motor. The stator windings are supplied with three phase sinusoidal voltage in Y-configuration in references [9, 10]. The authors in references [9, 10] neglect the impact of eddy current losses in the stator conductors. Reference [10] claims that misleading results are achieved if skin effect is included and the wire cross-sectional area of the elementary stator slot conductors is considered. Skin effect is included in the model of the solid rotor bar conductors in references [9, 10]. The stator frequency equals the rotor frequency in the time-harmonic study. The resistivity of the rotor bars, see *Equation 2-11*, is slip dependent in reference [9] to consider the rotor motion. Thus, the end-ring resistances in the lumped rotor end-ring circuit are divided with slip. Constant values of the velocity are inserted in the steady state simulations in reference [10]. A differential equation that describes the movement is implemented to get the rotational velocity at start-up.

Table 1-1 Main differences in references [9, 10].

Reference	Study	Ferromagnetic materials	Rotor cage
[9]:	Time-harmonic	Linear	Double
[10]:	Dynamic	Non-linear	Single

Table 1-2 Main similarities in references [9, 10].

2D/3D	U/I	Y/D	Use of symmetry	End-effects included
2D	U	Y	Yes	Yes

1.5 THESIS OBJECTIVES

The goal of this thesis work is to develop a 2D electromagnetic model of a specific induction motor in the finite element method based software-tool COMSOL Multiphysics version 4.4. COMSOL Multiphysics should be benchmarked with the computer software-tool FEMM. Simulation results of the torque must be compared with the torque, derived based on the equivalent circuit representation. The main intention is to couple the developed EM-model to an acoustic module for studying motor vibrations and noise levels as described in *Section 1.2.3*. This part is excluded due to the limited time of this thesis work. However, the air-gap forces should be calculated at the operating point (4.7% slip) to enable the connection to the vibratory analysis.

1.6 METHOD

A time-harmonic study of the induction motor is made to benchmark COMSOL Multiphysics with the finite element method based free software-tool FEMM. The geometry of the motor is simple. It is current supplied. End-effects are neglected and all materials are assumed to be linear. Simulation results are used to derive lumped circuit parameters. The circuit-derived torque is compared with the simulated torque. A time-dependent simulation at constant speed (4.7% slip) is made in COMSOL Multiphysics. The torque is compared to the result in the time-harmonic simulation and the air-gap forces are calculated according to *Section 2.11*. The used software-tools and type of studies in this thesis are summarized in *Table 1-3* and *Table 1-4*.

Table 1-3 Computer software-tools used in this thesis work.

Name	Description
COMSOL:	The electromagnetic model is developed in COMSOL Multiphysics. A time-harmonic analysis and a time-dependent simulation at the operating point (1430rpm) is made.
FEMM:	A time-harmonic simulation is made using this software-tool which is based on the finite element method.

Table 1-4 *Simulation studies in this thesis work.*

Type of study	Description
<i>Time-harmonic (frequency):</i>	Static simulations are made in the frequency domain with a varying slip frequency.
<i>Time-varying (dynamic):</i>	The time-varying study is made in the time domain at a constant speed.

1.7 THESIS OUTLINE

- Chapter 2:** The background theory is described in Chapter 2. The operation of the squirrel-cage induction motor is presented and the three-phase supply is also described. Chapter 2 also includes theory of the finite element method, skin effect and force calculation.
- Chapter 3:** An equivalent lumped model of the induction motor is presented in Chapter 3. An analytical expression of the torque is derived based on this electric circuit.
- Chapter 4:** The COMSOL-model of the induction motor is described in Chapter 4. It covers the geometry, boundary conditions, air-gap mesh and the equation that is solved in COMSOL Multiphysics.
- Chapter 5:** Simulation results obtained in the time-harmonic simulation (frequency domain) of the induction motor are presented and discussed in Chapter 5. COMSOL Multiphysics is benchmarked with FEMM.
- Chapter 6:** Results from the time-dependent simulation obtained in COMSOL Multiphysics at the operating point are presented in Chapter 6. The torque is compared with the results obtained in Chapter 5. The air-gap forces are evaluated.
- Chapter 7:** Conclusions drawn of this study and future work.

CHAPTER 2 FEM-MODEL OF A SQUIRREL-CAGE INDUCTION MOTOR

2.1 PRINCIPLE OPERATION OF A SQUIRREL-CAGE INDUCTION MOTOR

The induction motor (or asynchronous motor) consists of a laminated stator- and rotor-core. Squirrel-cage motors have axial rotor bars, often casted with aluminum or copper [3], connected to two short circuited end-rings. [11] Symmetrical three phase voltages, displaced by 120° (electrical), are supplied on the stator windings. Electric current flows through the stator conductors and causes a magnetic field that rotates with synchronous speed. At no-load operation the rotor frequency equals the stator frequency and current is not induced in the rotor bars. However, current is generated in the rotor bars as the rotor frequency decreases. The rotor bar currents induce an interacted magnetic field. Torque is produced only if the rotor moves with a slightly lower speed relative to the stator.

2.2 ROTOR BAR TOPOLOGY

There are different geometric structures of the rotor bars. The rotor slots are designed in different ways to handle inverter supply or sinusoidal supply [12].

The single- and the double- cage rotors are illustrated in *Figure 2-1 (a), (b) and (c)*. The most common rotor bar shape is the single cage rotor [3]. Double-cage rotors are suitable for motors connected to the grid. The starting torque (or locked rotor torque) is higher for the double-cage rotor compared to the single-cage rotor since the rotor-resistance of the former is higher at the grid-frequency. [3, 13]

Closed rotor bars, *Figure 2-1 (b) and (c)*, are unlike open rotor bars, *Figure 2-1 (a)* enclosed with ferromagnetic material that forms bridges over the bar openings. These are often used in motors up to 250kW [14]. The rotor bar conductors are kept in place and aluminum is prevented from leaking on the rotor surface during the rotor casting [3, 14].

Stray losses are reduced for closed rotor bars. The starting torque is lower compared to open rotor bars since the slot leakage is higher. [3]

A comparison of open- and closed- rotor bars of a 45kW, 4-pole induction motor is made in reference [14]. Time dependent FEM-simulation results indicate that the level of stator vibrations increase, for frequencies above 1kHz, for open bars. The reason is because the impact of the stator current harmonics is higher compared to closed rotor bars. The rotor bridge is considered in the equivalent circuit in reference [3] by adding a voltage source on the rotor side.

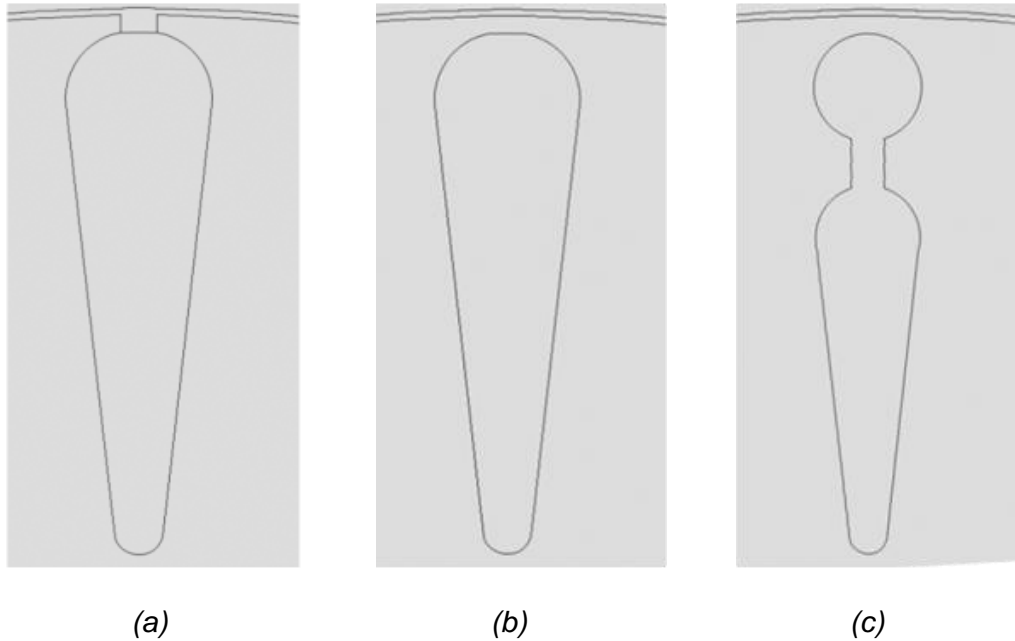


Figure 2-1 Single-cage rotor with an: (a) open rotor bar, (b) closed rotor bar. (c) Double-cage rotor.

2.3 SINUSOIDAL VOLTAGE SUPPLY ON A THREE-PHASE WINDING ARRANGEMENT

It is assumed that the induction motor is supplied with balanced three-phase sinusoidal supply. Three-phase windings are placed in the stator slots to create the moving magnetic field when the motor is supplied with symmetrical three-phase voltages. *Figure 2-2 (a)* shows how the phases are distributed in the motor and the rotors moving direction (anti-clockwise). Distributed windings are used in induction motors. The windings could have different number of layers. Single and double layer windings are common. *Figure 2-2 (b)* shows a single layer winding configuration with $q=3$ slots per pole and phase. The pole-pitch, τ_p is spanning over 9 slots. Single layer windings have no fractional pitch. Each slot contains one coil side. Small (AC) motors have single layer windings [15]. A three phase concentric winding is an example of a single layer winding.

Equation 2-1, *Equation 2-2* and *Equation 2-3* describe a symmetrical three phase voltage system. Stationary solutions are obtained by fixing the time to constant values.

$$V_a = \hat{V} \cdot \cos(\omega t), \quad \text{Equation 2-1}$$

where \hat{V} is the peak-value of the stator voltage, V_a is the stator voltage supply in phase A, ω is the angular speed and t is the time.

$$V_b = \hat{V} \cdot \cos\left(\omega t - \frac{2\pi}{3}\right), \quad \text{Equation 2-2}$$

where V_b is the stator voltage supply in phase B.

$$V_c = \hat{V} \cdot \cos\left(\omega t + \frac{2\pi}{3}\right),$$

Equation 2-3

where V_c is the stator voltage supply in phase C.

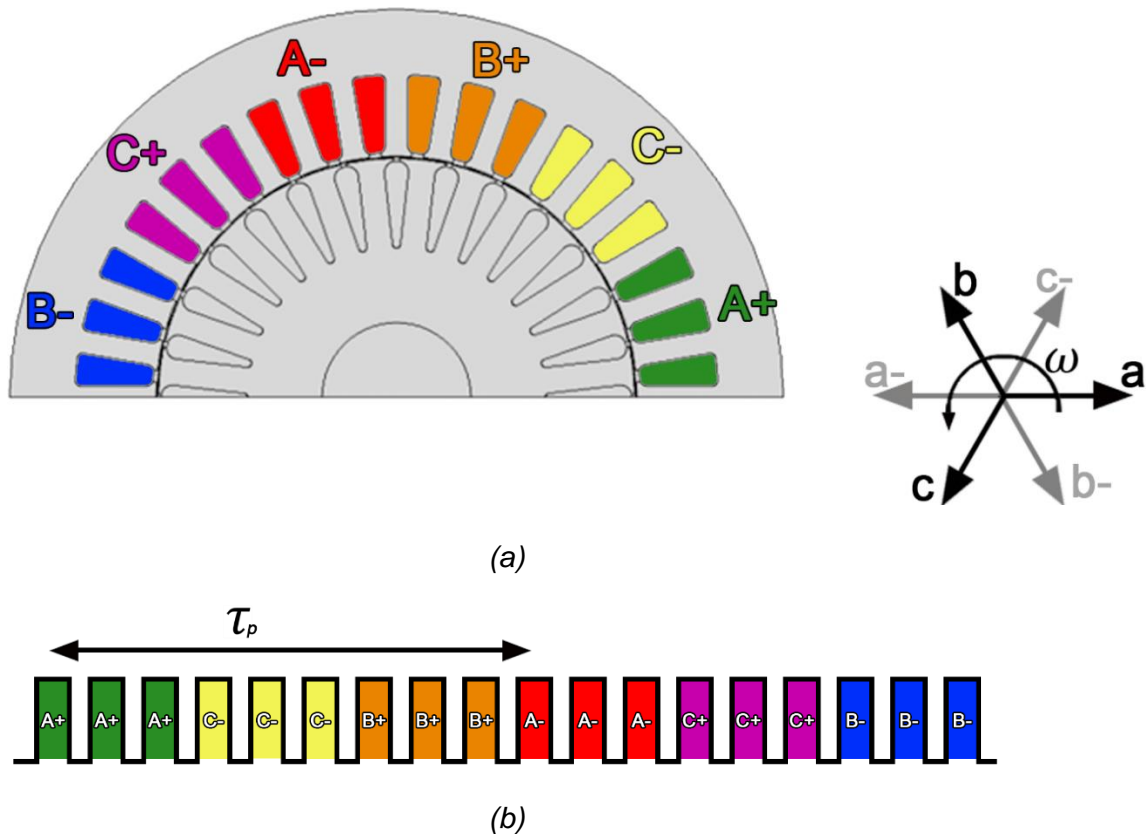


Figure 2-2 (a) Three-phase winding arrangement over 2 poles (one pole pair). (b) Single layer winding, $q = 3$ slots per pole and phase.

2.4 CONNECTION OF THE STATOR WINDING PHASES

The three phase windings could be fed with voltage or current and coupled in either Y - or Δ - configuration. *Figure 2-3 (a)* illustrates how the voltage-fed stator windings are coupled in Y -connection and *Figure 2-3 (b)* in Δ - configuration. V_{ba} and V_{ac} are line-to-line voltages between phase B and A and phase A and C.

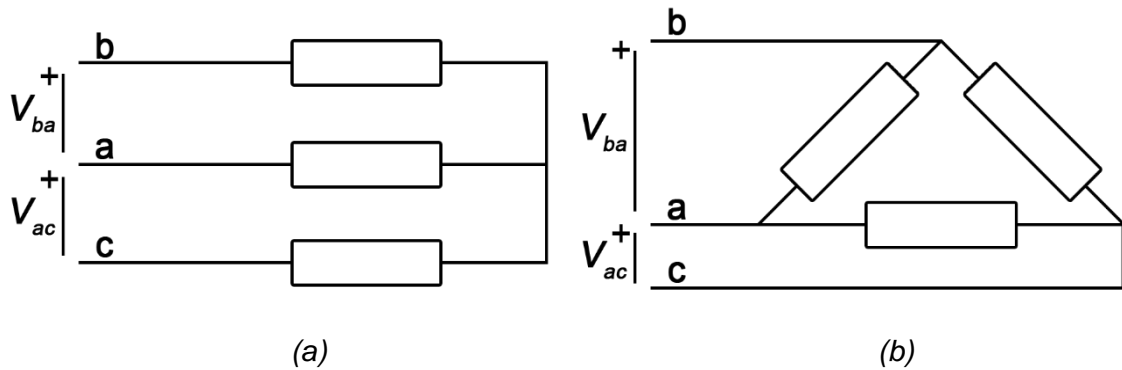


Figure 2-3 (a) Y - and (b) Δ - connection of the voltage-fed stator winding.

2.5 MAGNETIZATION CURVE

The external applied magnetic field intensity has a linear dependency ($B = \mu_r \mu_0 \cdot H$) in relation to the magnetic flux density as shown in *Figure 2-4 (b)*, where the magnetic permeability obtains a constant value. However, ferromagnetic materials could get saturated. Saturation is included in the BH-curve in *Figure 2-4 (a)*. The magnetization curve is symmetric. The flux density increases slowly or remains constant when saturation is reached and the magnetic field intensity is increased. The average curve is denoted in red in *Figure 2-4 (a)*. The area of the BH-curve is proportional to the hysteresis losses. B_r is the remanent magnetic flux density and H_c is the coercive field strength.

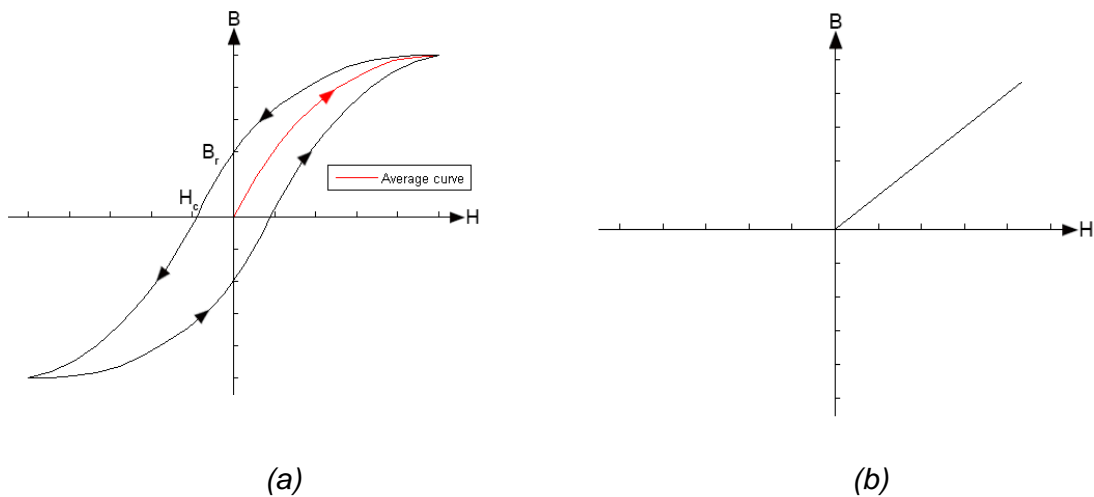


Figure 2-4 (a) Magnetization curve. (b) Linear region of a BH-curve.

2.6 TRIANGULAR MESH IN A 2D PROBLEM FORMULATION

The finite element method is used to estimate solutions of physical problems. The domain is discretized with finite elements. It consists of triangular elements in a two-dimensional problem formulation. *Figure 2-5* shows how the triangular mesh is distributed in the air-gap. The highlighted part of the air-gap shows that the sides of the triangles are ideally equal. An increased number of elements result in more degrees of freedom and longer computational time. δ is the air-gap thickness.

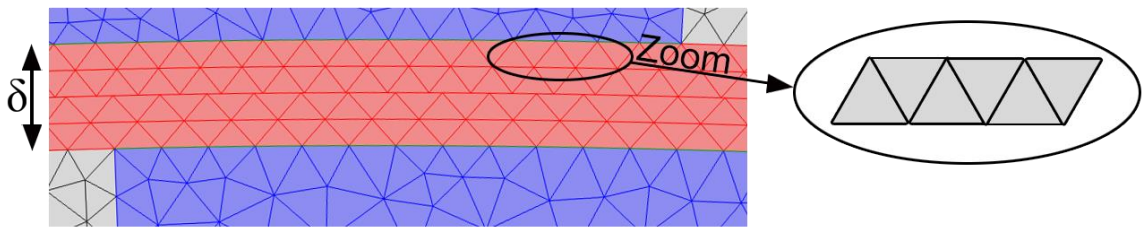


Figure 2-5 Distribution of the triangular mesh in a part of the air-gap.

2.7 DIFFERENTIAL FORM OF MAXWELL'S EQUATIONS

Maxwell's equations, see *Equation 2-4* to *Equation 2-7*, are combined in FEM software-tools to find approximate solutions to the discretized finite elements. A rotating electric field is induced when there is a time-varying magnetic flux density according to *Equation 2-4*, which is called Faraday's law. *Equation 2-5* describes Ampere's law. The expression of the displacement current is neglected since the electromagnetic fields are assumed to be quasi-static (which is valid for frequencies below tens of kHz [16]) [17]. Gauss's law is given in *Equation 2-6*. *Equation 2-7* describes that there are no magnetic charges [17] and that the magnetic field-lines form closed loops.

$$\nabla \times \mathbf{E} = -\frac{\partial \mathbf{B}}{\partial t}, \quad \text{Equation 2-4 [16]}$$

where \mathbf{E} is the electric field (vector form) and \mathbf{B} is the magnetic flux density (vector form).

$$\nabla \times \mathbf{H} = \mathbf{J} + \frac{\partial \mathbf{D}}{\partial t} \approx \mathbf{J}, \quad \text{Equation 2-5 [16]}$$

where \mathbf{H} is the magnetic field intensity (vector form) and \mathbf{J} is the current density (vector form) and \mathbf{D} is the electric displacement field (vector form).

$$\nabla \cdot \mathbf{D} = \rho, \quad \text{Equation 2-6 [16]}$$

where ρ is the electric charge density.

$$\nabla \cdot \mathbf{B} = 0 \quad \text{Equation 2-7 [16]}$$

2.8 MAGNETIC VECTOR POTENTIAL

The magnetic vector potential in *Equation 2-8* is solved in every node in a two-dimensional problem formulation. *Equation 2-9* shows that the magnetic flux density is the curl of the magnetic vector potential.

$$\mathbf{A} = A(x, y) \cdot \mathbf{e}_z, \quad \text{Equation 2-8 [16]}$$

where \mathbf{A} is the magnetic vector potential (vector form), \mathbf{e}_z is the unit vector in the z -direction.

$$\mathbf{B} = \nabla \times \mathbf{A} \quad \text{Equation 2-9 [10]}$$

2.9 STATOR FLUX LINKAGE

The stator flux linkage per phase is complex valued in the frequency domain. It is computed in the stator slots by integrating the magnetic vector potential in each phase using *Equation 2-10*.

$$\psi_s = \frac{N_t \cdot L}{A_{ss}} \cdot \left(\int_{+Q_s} A_z dS - \int_{-Q_s} A_z dS \right), \quad \text{Equation 2-10 [10]}$$

where ψ_s is the stator flux linkage per phase, N_t is the number of turns per stator slot, A_{ss} is the stator slot area, L is the lamination length, $+Q_s$ and $-Q_s$ are the stator slots with positive- and negative- direction of the current density, A_z is the magnetic vector potential and S is the surface.

2.10 SKIN EFFECT

Skin effect appears for example in the rotor bars when alternating current flows through them. The current density and the flux density are not evenly distributed in the bars. The distribution of the current gets more concentrated around the top of the bars [3]. *Equation 2-11* illustrates the skin depth, which is proportional to the square root of the bar resistivity times the inverse of the frequency. The skin depth is increased as the frequency is reduced and/or the bar resistivity is increased (decreased conductivity). Skin effect is zero if the electric conductivity is neglected.

$$\delta_{skin} = \sqrt{\frac{\rho_{bar}}{\mu_0 \cdot \pi \cdot f}} \quad \text{Equation 2-11 [3]}$$

where δ_{skin} is the skin depth, ρ_{bar} is the rotor bar resistivity and f is the frequency.

2.11 FORCE-CALCULATION

The force calculation domains are marked in green in *Figure 2-6*. These regions must be enclosed by air to get accurate results of the torque [18]. The electromagnetic torque is computed by a volume integration of Maxwell's stress tensor over the selected area [18]. An average valued torque (or weighted torque) is calculated in the time-harmonic simulations (frequency domain). In reference [19] a method is described on how to compute radial magnetic forces based on FEM-results of the air-gap flux density. The red arc-line in *Figure 2-6* is placed in the middle of the air-gap. The Maxwell's stress tensor is used to calculate the radial- and tangential- air-gap forces in *Equation 2-12* and *Equation 2-13* [19]. These forces could be used for studying motor vibrations.

$$\sigma_r = \frac{1}{2\mu_0} (B_n^2 - B_t^2), \quad \text{Equation 2-12 [19]}$$

where σ_r is the radial magnetic force, B_n is the normal component of the magnetic flux density, B_t is the tangential component of the magnetic flux density.

$$\sigma_t = \frac{1}{\mu_0} (B_n \cdot B_t), \quad \text{Equation 2-13 [19]}$$

where σ_t is the tangential magnetic force. Unit conversion from N/m^2 to N is obtained by integrating the force densities in *Equation 2-12* and *Equation 2-13* over the arc line and multiplying with the active motor length.

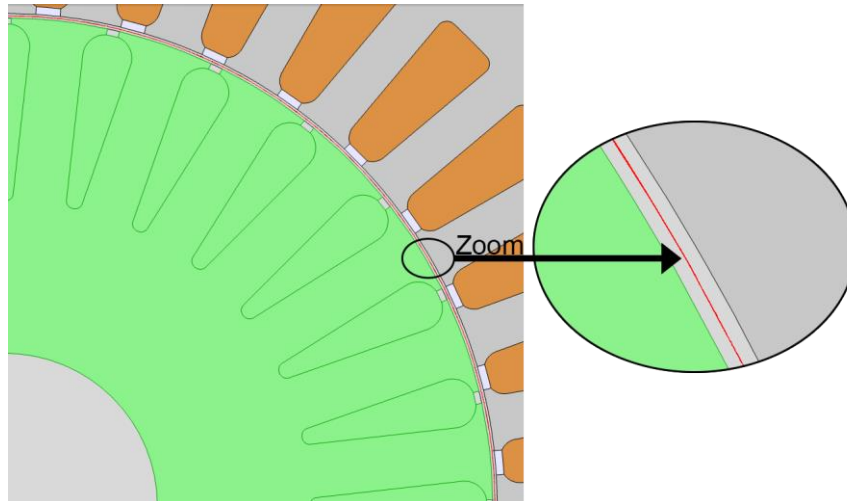


Figure 2-6 Force-calculation surface and line.

CHAPTER 3 LUMPED MODEL OF THE INDUCTION MOTOR

3.1 SIMPLIFIED ELECTRIC CIRCUIT

The electric circuit representation of the induction motor is seen in *Figure 3-1*. This lumped element circuit is used to show that the simulation results of the torque is comparable with the circuit based analysis. The end-winding impedance, rotor end-ring impedance and skin effect of the rotor are not included in the equivalent circuit of the motor. Furthermore, the rotor leakage is included in the stator leakage. Point-values of the stator flux linkage are achieved from the FEM-simulations of the induction motor. A curve fit of the imaginary part of the phase inductance is made to find the solution that minimizes the error in *Equation 3-6*. The results are used to determine the parameters of the per phase (steady state) circuit. The circuit parameters in *Figure 3-1* are V_s = stator supply voltage, i_s = stator phase current, i_M = magnetizing current, i'_r = rotor current, R_s = stator resistance, $L_{\lambda s}$ = stator leakage inductance, L_M = mutual inductance, R'_r = rotor resistance and s = slip.

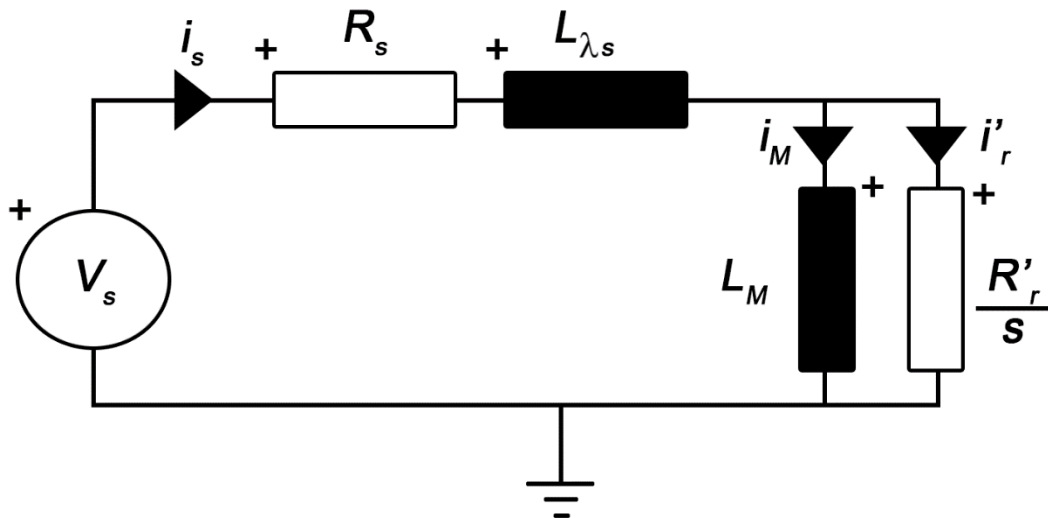


Figure 3-1 Simplified equivalent circuit per phase of the induction motor at steady state.

3.2 ELECTRIC-CIRCUIT BASED ANALYSIS

This section is based on reference [20]. The slip in *Equation 3-1* is the ratio of the difference between the stator- and rotor- angular frequency relative the stator angular frequency.

$$s = \frac{\omega_s - \omega_m}{\omega_s} = \frac{\omega_1 - p_p \cdot \omega_m}{\omega_1} = \frac{\omega_{slip}}{\omega_1}, \quad \text{Equation 3-1}$$

where ω_s = angular speed of stator, mech.rad/s, ω_m = angular speed of rotor, mech.rad/s, p_p = number of pole pairs, ω_1 = angular speed of stator, el.rad/s, ω_{slip} = angular slip frequency, rad/s. The rotor time constant, τ is defined in *Equation 3-2*.

$$\tau = \frac{L_M}{R'_r} \quad \text{Equation 3-2 [20]}$$

The total phase impedance, Z_{phase} in *Equation 3-3* is achieved using electric circuit theory.

$$Z_{phase} = \frac{V_s}{I_s} = R_s + j\omega_1 \cdot L_{phase} , \quad \text{Equation 3-3}$$

where j is the imaginary unit and L_{phase} is the phase inductance. The phase inductance in *Equation 3-3* is complex-valued. It is separated into its real- and imaginary- part in *Equation 3-4*.

$$L_{phase}(\omega_{slip}) = \frac{\psi_s}{I_s} = L_{\lambda s} + \frac{L_M}{1 + (\omega_{slip} \cdot \tau)^2} - j \cdot \frac{\omega_{slip} \cdot \tau \cdot L_M}{1 + (\omega_{slip} \cdot \tau)^2} \quad \text{Equation 3-4 [20]}$$

The components of the real- and the imaginary- phase inductance named L_r and L_i are introduced in *Equation 3-5*.

$$L_{phase} = \Re(L_{phase}(\omega_{slip})) + j \cdot \Im(L_{phase}(\omega_{slip})) \rightarrow$$

$$\rightarrow \begin{cases} L_r = \Re(L_{phase}(\omega_{slip})) = L_{\lambda s} + \frac{L_M}{1 + (\omega_{slip} \cdot \tau)^2} \\ L_i = \Im(L_{phase}(\omega_{slip})) = -\frac{\omega_{slip} \cdot \tau \cdot L_M}{1 + (\omega_{slip} \cdot \tau)^2} \end{cases} \quad \text{Equation 3-5 [20]}$$

Point-values of L_r and L_i are known from simulation results. The expression of the imaginary part of the phase inductance in *Equation 3-5* is describing an over-determined system of equations. This is seen in *Equation 3-6* by introducing the constant values that minimize the error c_1 and c_2 when the slip frequency is varied. The circuit parameters are determined based on the values of these constants. The stator resistance is evaluated from the resistive losses at no-load operation (zero slip) [21].

$$\text{Equation 3-5} \rightarrow -L_i = \begin{cases} c_1 = \tau \cdot L_M \\ c_2 = \tau^2 \end{cases} = \omega_{slip} \cdot c_1 + L_i \cdot \omega_{slip}^2 \cdot c_2 \quad \text{Equation 3-6 [21]}$$

The three phase air-gap power, P_δ is seen in *Equation 3-7* [13].

$$P_\delta = 3 \cdot \frac{R'_r}{s} \cdot |i'_r|^2 \quad \text{Equation 3-7 [13]}$$

The air-gap power in *Equation 3-7* consists of the resistive losses in the rotor and the mechanical output power. The latter is used to obtain the electromagnetic torque, T_e . The delivered mechanical three-phase power, P_{mech} is given in reference [13] as:

$$P_{mech} = (1 - s) \cdot P_\delta \quad \textbf{Equation 3-8 [13]}$$

The electromagnetic torque of the induction motor, see *Equation 3-9*, is the mechanical output power relative the mechanical angular frequency.

$$T_e = \frac{P_{mech}}{\omega_m} = 3 \cdot \frac{p_p}{\omega_{slip}} \cdot R'_r \cdot |i'_r|^2 \quad \textbf{Equation 3-9 [20]}$$

The torque in *Equation 3-9* is written as a function of the RMS-value of the stator phase current in *Equation 3-13*. KCL is used in *Equation 3-10*.

$$i_s = i_M + i'_r \quad \textbf{Equation 3-10 [20]}$$

i_M is expressed in terms of i'_r in *Equation 3-11*. The voltage over the rotor resistance equals the voltage over the magnetizing inductance.

$$i_M = \left(\frac{1}{j\omega_1 L_M} \right) \cdot \frac{R'_r}{s} \cdot i'_r \quad \textbf{Equation 3-11}$$

Equation 3-12 is obtained by inserting *Equation 3-11* into *Equation 3-10*. *Equation 3-1* and *Equation 3-2* are also applied to get the expression in *Equation 3-12*.

$$\textbf{Equation 3-10} \rightarrow i'_r = \frac{j\omega_{slip}\tau}{1+j\omega_{slip}\tau} \cdot i_s \quad \textbf{Equation 3-12 [20]}$$

Inserting *Equation 3-12* into *Equation 3-9* yields to the torque expression in *Equation 3-13*.

$$\textbf{Equation 3-9} \rightarrow T_e = 3 \cdot p_p \cdot L_M \cdot |i_s|^2 \cdot \frac{\omega_{slip}\tau}{1+(\omega_{slip}\tau)^2} \quad \textbf{Equation 3-13 [20]}$$

CHAPTER 4 FEM-MODEL OF THE IM IN COMSOL MULTIPHYSICS

4.1 DESCRIPTION OF THE STUDIED INDUCTION MOTOR

Figure 4-1 (a) shows the cross-section of the investigated motor. It is a single-cage induction motor with an open rotor bar topology. Motor-data is found in *Table A-1*. The motor consists of 36 stator slots, 28 rotor slots and 4 poles. The time-harmonic simulations in FEMM are made using the geometry in *Figure 4-1 (b)* which covers one pole pitch of the induction motor. Periodic boundary conditions seemed to cause trouble in the time-stepper according to the COMSOL Support Team. Therefore, it was decided to simulate the whole cross-section (360° mechanical) in COMSOL Multiphysics instead of using anti-periodic boundary conditions. A current fed approach is chosen even though induction motors are in general voltage fed. The end-winding impedance is not included in the model. Simulations are made with 1A (peak) supply. The stator windings are connected in Y-configuration. The time-harmonic simulations in reference [20] are also made with 1A supply and Y-connected stator windings. The rotor bars are coupled in parallel and short-circuited. Skin effect is included in the rotor bars in the FEM-model but excluded in the equivalent circuit in *Figure 3-1*. The ferromagnetic materials are assumed to be linear with the relative magnetic permeability 7000. The eddy current losses and skin depth of the iron material are disregarded since the purpose of this thesis work is not to investigate the iron losses.

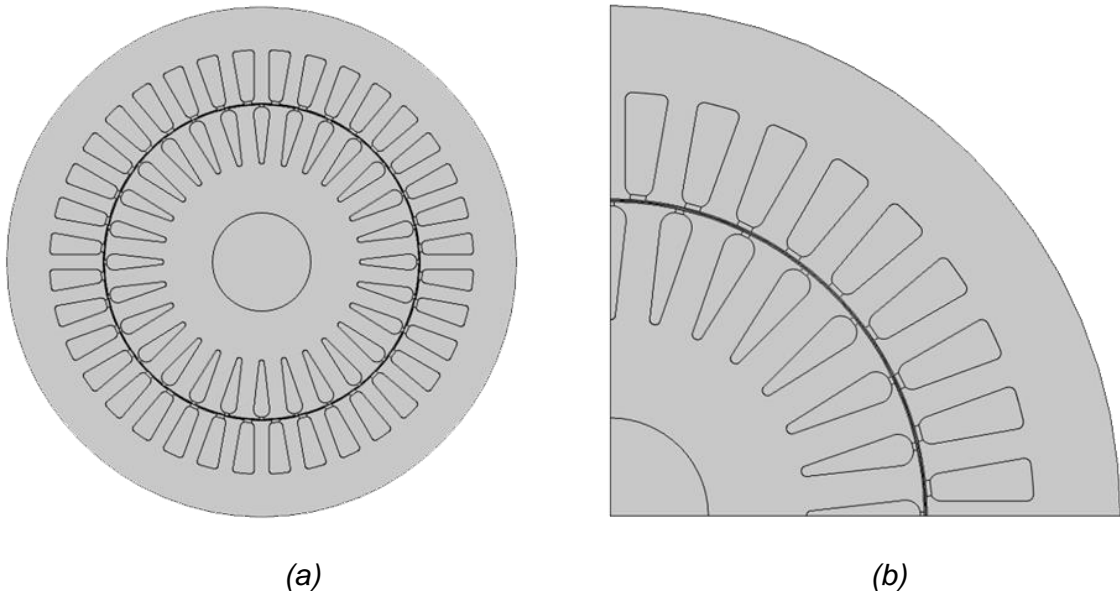


Figure 4-1 (a) Cross-section of the induction motor with 4 poles, (b) smallest possible symmetry covering one pole-pitch of the motor.

4.2 BOUNDARY CONDITIONS

The rotor-domain and half of the air-gap forms an assembly for the rotating part in the COMSOL-model of the IM. The fixed part includes the second half of the air-gap and the stator-domain. Continuity is applied on the intersected boundary placed in the middle of the air-gap. This method for dividing the motor geometry in assemblies was described in the model library in COMSOL Multiphysics. Magnetic insulation is applied on the outer motor-diameter and around the boundary of the shaft.

4.3 MATERIAL

Table 4-1 illustrates the materials of the motor. The stator conductors are made of copper. Each slot contains of 44 turns. The rotor bars are casted with aluminum with the electric conductivity 34.45MS/m. The ferromagnetic material is made of lossless iron.

Table 4-1 *Defined materials of the studied induction motor.*

Part:	Material:
Stator- and rotor- core:	Soft iron (lossless)
Stator conductors:	Copper
Rotor bars:	Aluminum

4.4 ELEMENT QUALITY OF THE MESH

The element quality in 2D is described by *Equation 4-1*. It indicates the quality of the mesh. The equation is received from reference [22]. The element quality of a triangle is defined on a scale that reaches from 0 (*low*) to 1 (*high*) in COMSOL Multiphysics. The mesh quality is influencing the convergence of a numerical problem [22]. The minimum element quality specifies the poorest quality of the triangular elements.

$$q_{\Delta} = \frac{4 \cdot \sqrt{3} \cdot A_{\Delta}}{\sum_{k=1}^3 l_{k,\Delta}^2}, \quad \text{Equation 4-1 [22]}$$

where A_{Δ} , $l_{k,\Delta}$ and q_{Δ} denote the area, length of side $k = 1, \dots, 3$ and the quality per triangular element [22].

4.5 AIR-GAP MESH DENSITY

It is important to have a high air-gap mesh density to get accurate results of the torque, according to reference [21]. Thus, the air-gap element-size of the motor was swept relative the torque at a fixed slip value in COMSOL Multiphysics. However, the torque did not converge as the mesh density increased. Therefore, simulations were made for a coarse- and a refined- mesh, see *Figure 4-2 (a)* and *(b)*. *Table 4-2* shows that the refined mesh contains over three times more triangular elements in the air-gap compared to the coarse-mesh. The minimum element quality, defined in *Section 4.4*, of the air-gap elements is over 400 times more for the refined- compared to the coarse- mesh. It was decided to use the refined mesh for the simulations in Chapter 5 and Chapter 6 after comparing the torque obtained in COMSOL Multiphysics with the results obtained in FEMM.

Table 4-2 Coarse- and refined- triangular mesh in the air-gap.

Type of mesh	Number of air-gap elements	Minimum quality of the air-gap elements
Coarse:	3981	0.002
Refined:	12672	0.833

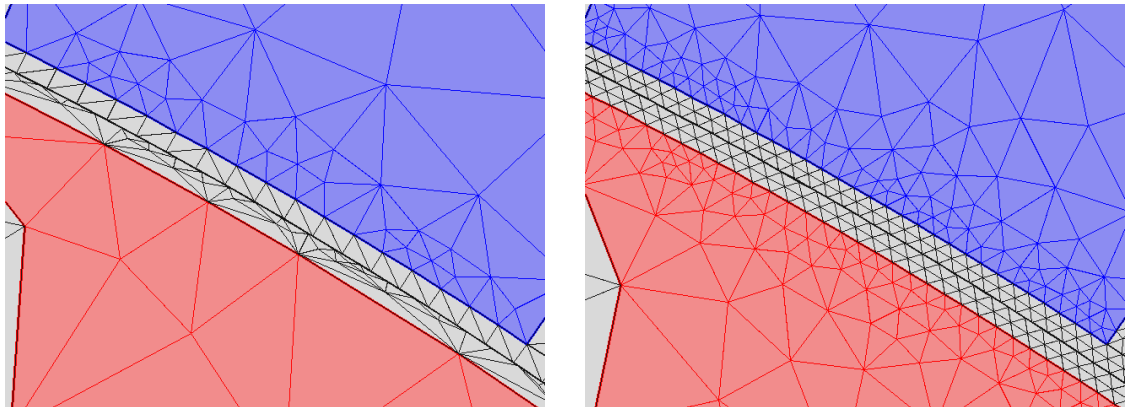


Figure 4-2 Section of the: (a) coarse- and (b) refined- triangular air-gap mesh of the IM.

4.6 SOLVED EQUATION

Equation 4-2 is solved in the time-dependent simulation in COMSOL Multiphysics. The corresponding equation for the simulation in the frequency domain is obtained by replacing the time derivative with $j\omega$. The $j\omega$ -method is applicable since the supply is assumed to be sinusoidal.

$$\sigma \cdot \frac{\partial \mathbf{A}}{\partial t} + \nabla \times \mathbf{H} - \sigma \cdot \mathbf{v} \times \mathbf{B} = \mathbf{J}, \quad \text{Equation 4-2 [10]}$$

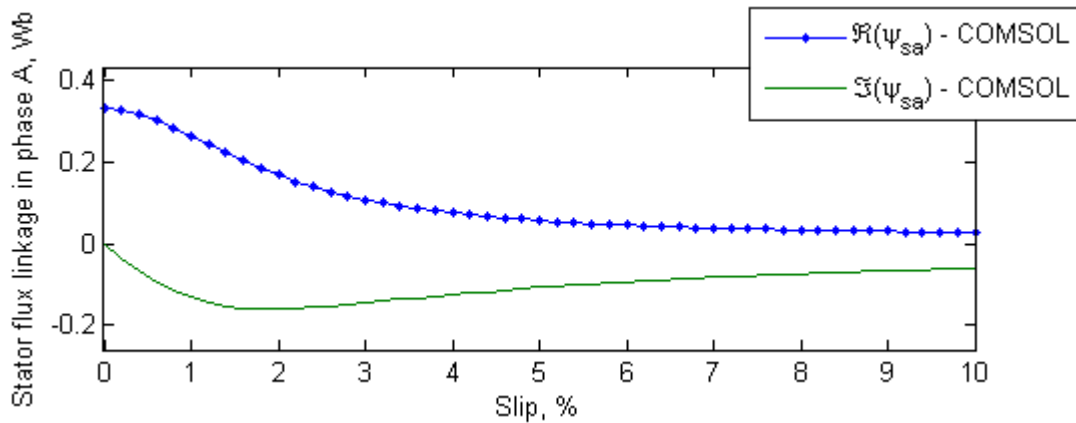
where σ is the electrical conductivity and \mathbf{v} is the velocity (vector form).

Chapter 5 TIME-HARMONIC SIMULATION OF THE INDUCTION MOTOR

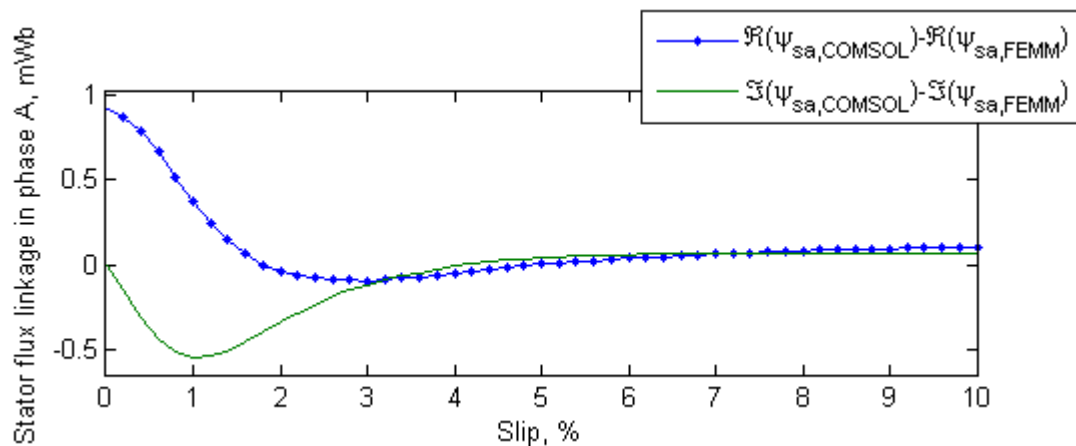
This chapter contains results from the time-harmonic simulations of the IM. COMSOL Multiphysics is benchmarked with FEMM. The equivalent circuit in Chapter 3 is used to validate the simulated torque. The simulations are made in the frequency domain. Several static simulations are made to get the performance at different rotor positions.

5.1 STATOR FLUX LINKAGE IN PHASE A

The complex valued components of the stator flux linkage of phase A, ψ_{sa} in Figure 5-1 (a) are achieved, using Equation 2-10, when the motor is supplied with 1A (peak). The deviation in radial- and tangential- stator flux linkage between results obtained in COMSOL Multiphysics and FEMM is below 0.001Wb which is seen in Figure 5-1 (b).



(a)

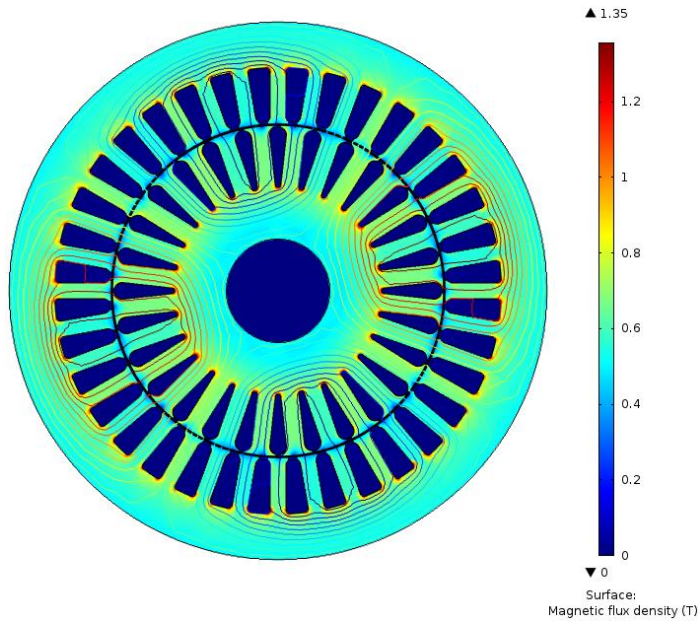


(b)

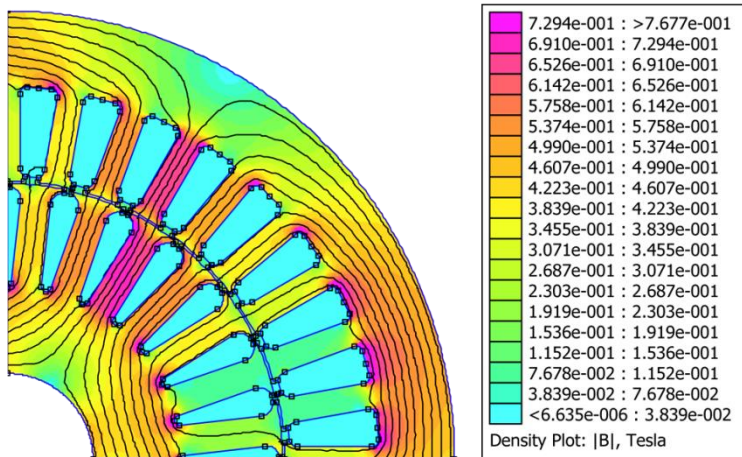
Figure 5-1 (a) Stator flux linkage per phase when the motor is supplied with 1A (peak). (b) Deviation in ψ_{sa} between COMSOL Multiphysics and FEMM.

5.2 DISTRIBUTION OF THE MAGNETIC FLUX DENSITY

The magnetic field distribution in COMSOL Multiphysics and FEMM at no-load operation is shown in *Figure 5-2 (a) and (b)*. The contour lines represent the magnetic vector potential and the surface plot is the flux density. The magnetic flux density is higher close to sharp edges.



(a)



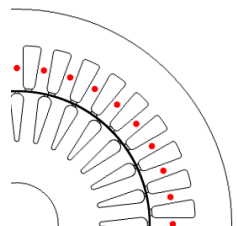
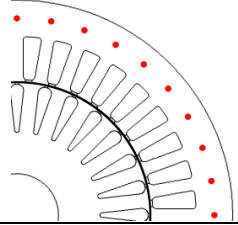
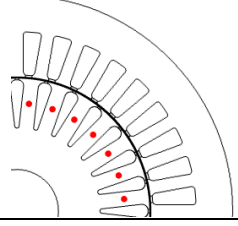
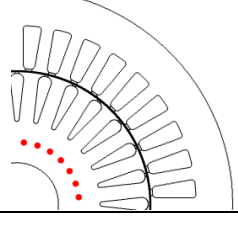
(b)

Figure 5-2 Surface plot of the magnetic flux density (T) and contour lines of the magnetic vector potential (Wb/m) at no-load in (a) COMSOL Multiphysics, (b) FEMM.

5.3 POINT-EVALUATION OF THE MAGNETIC FLUX DENSITY

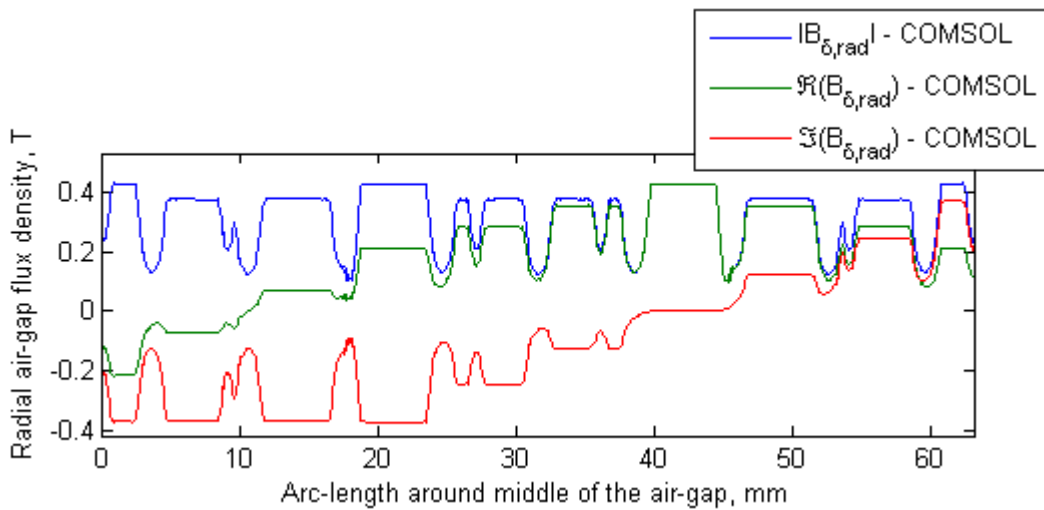
Table 5-1 includes the maximum point value, at no-load ($s = 0\%$), of the flux density at different locations of the stator and of the rotor. \hat{B}_r and \hat{B}_t are the radial- and the tangential-components of the maximum magnetic flux density (average value). The average point-value in COMSOL and FEMM are corresponding in the stator tooth and in the rotor back. However, the tangential flux density in the stator back is 0.63% higher in FEMM compared to COMSOL Multiphysics. The radial part of the magnetic flux density in the middle of the rotor tooth is 0.28% lower in FEMM compared to COMSOL Multiphysics.

Table 5-1 Maximum value of the B-field at different regions at no-load operation (average value).

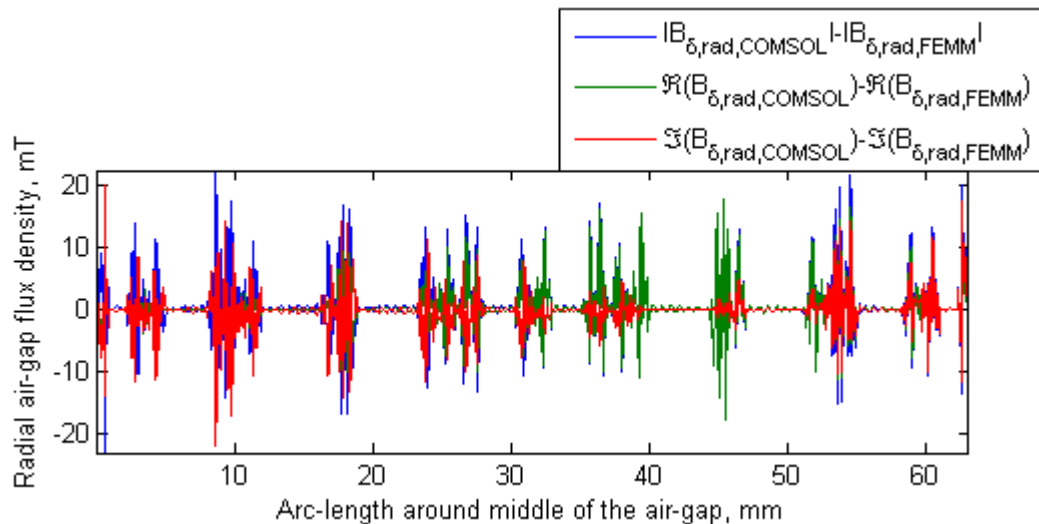
Position:	Flux density:	COMSOL:	(FEMM-COMSOL)/FEMM:	Location:
Stator tooth:	\hat{B}_r	0.293T	0%	
	\hat{B}_t	-0.002T	0%	
Stator back:	\hat{B}_r	0.055T	0%	
	\hat{B}_t	0.158T	+0.63%	
Rotor tooth:	\hat{B}_r	0.358T	-0.28%	
	\hat{B}_t	-0.001T	0%	
Rotor back:	\hat{B}_r	0.170T	0%	
	\hat{B}_t	-0.146T	0%	

5.4 AIR-GAP FLUX DENSITY AT NO-LOAD

The flux density consists of a radial- and an imaginary- part. *Figure 5-3 (a)* shows the radial flux density in the middle of the air-gap in COMSOL Multiphysics at no-load operation. $B_{\delta,rad}$ is the radial flux density spanning over one pole-pitch around the middle of the air-gap. *Figure 5-3 (b)* shows that the difference between the absolute value of the radial air-gap flux density in COMSOL compared to simulation results in FEMM is below 0.03T. The tangential part of the air-gap flux density at no-load operation and around one pole-pitch in COMSOL is seen in *Figure 5-4 (a)*. $B_{\delta,tang}$ is the tangential flux density covering one pole-pitch in the middle of the air-gap. The difference between simulation results in COMSOL and FEMM regarding the absolute valued tangential flux density is below 0.02T, see *Figure 5-4 (b)*.

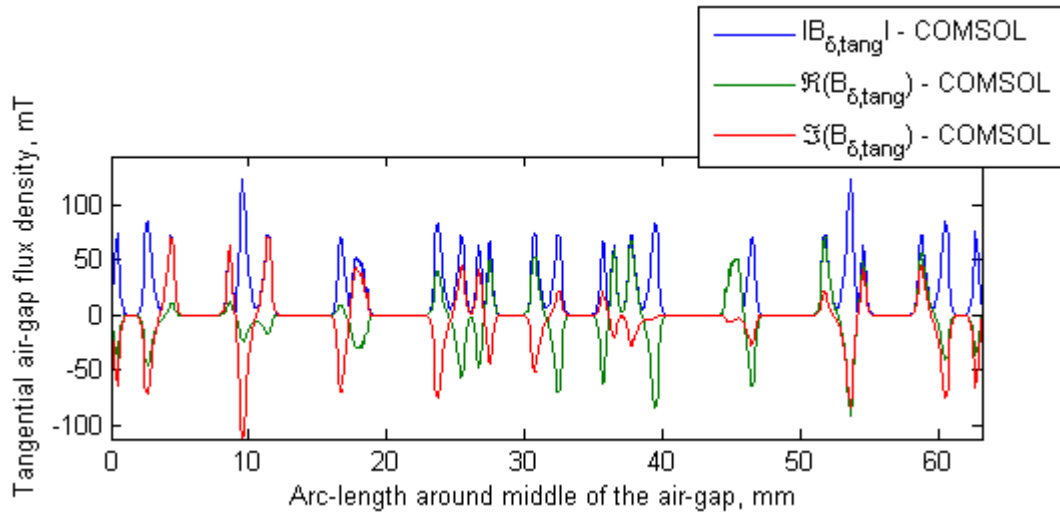


(a)

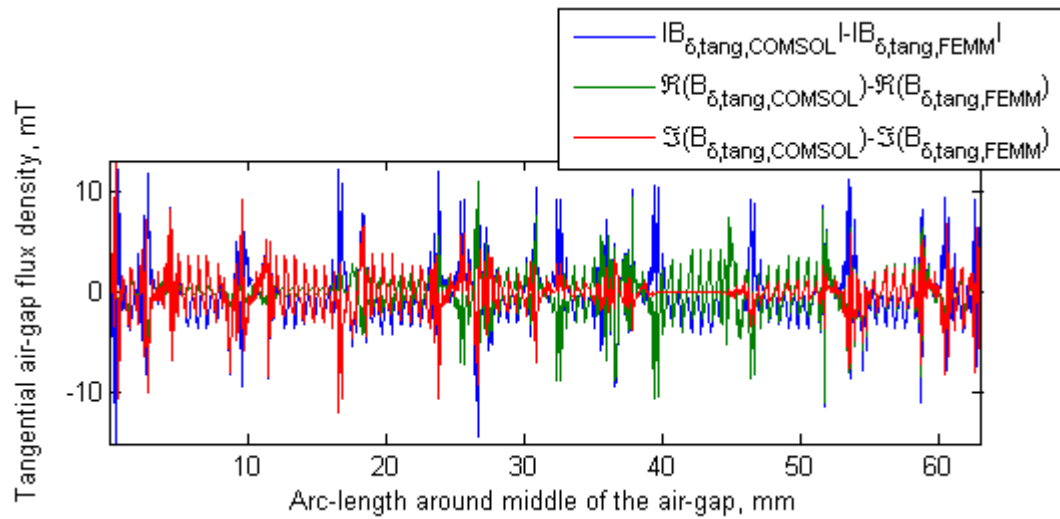


(b)

Figure 5-3 (a) Radial component of the magnetic flux density at no-load. (b) Difference between results of the radial flux density in COMSOL Multiphysics and FEMM.



(a)

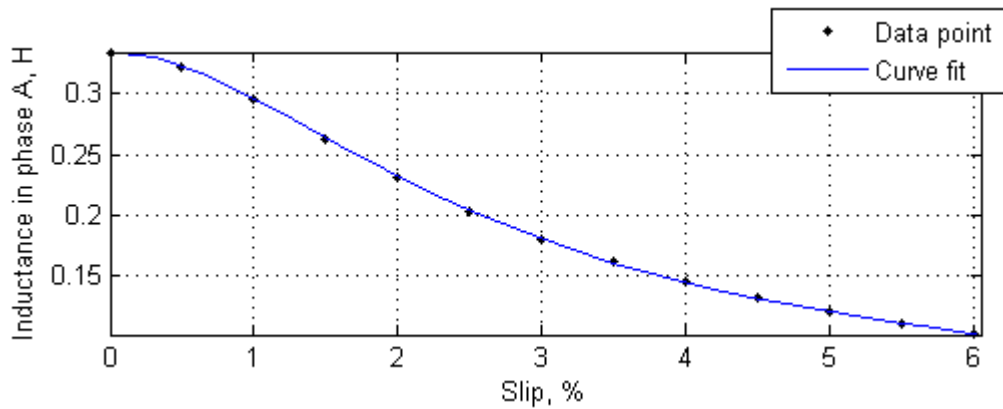


(b)

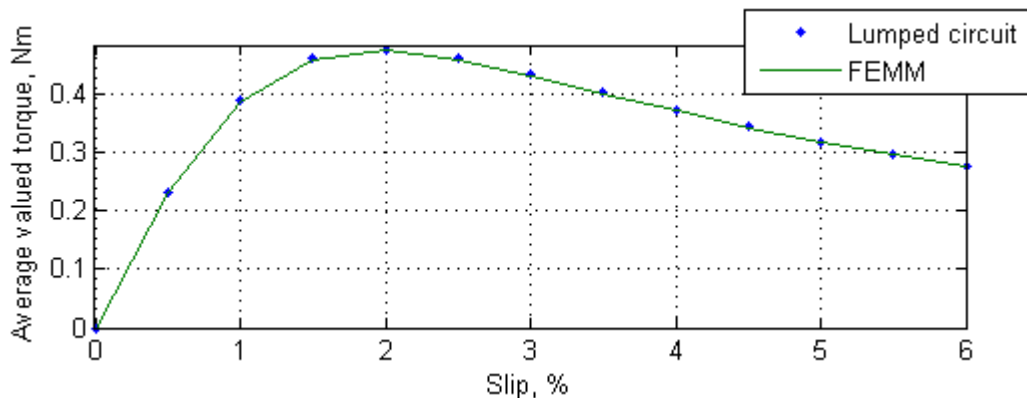
Figure 5-4 (a) Tangential component of the flux density at no-load. (b) Deviation in the tangential flux density between results obtained in COMSOL Multiphysics and FEMM.

5.5 VALIDATION OF THE SIMULATED TORQUE

The values of the phase inductance, up to 6% slip, labeled “Data point” in *Figure 5-5 (a)* and *Figure 5-6 (a)* are deduced from simulation results of the stator flux linkage and current, see *Equation 3-4*. Circuit analysis is applied on the lumped model in *Figure 3-1* to derive *Equation 3-6*. The phase inductance in *Equation 3-5* is calculated based on the solution that minimizes the error of the over-determined system of equations. The curves labeled “Curve fit” in *Figure 5-5 (a)* and *Figure 5-6 (a)* are achieved based on circuit theory. The simulated average valued torque is shown in *Figure 5-5 (b)* in FEMM and *Figure 5-6 (b)* in COMSOL Multiphysics. The corresponding torque based on the electric circuit relations in *Equation 3-13* is labeled “Lumped circuit”. The maximum deviation between simulated and analytical torque is 0.002Nm in FEMM and 0.009Nm in COMSOL Multiphysics.

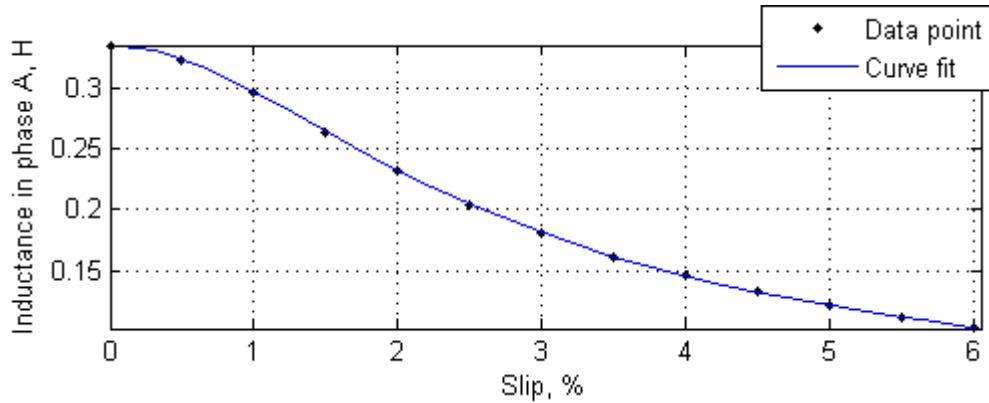


(a)

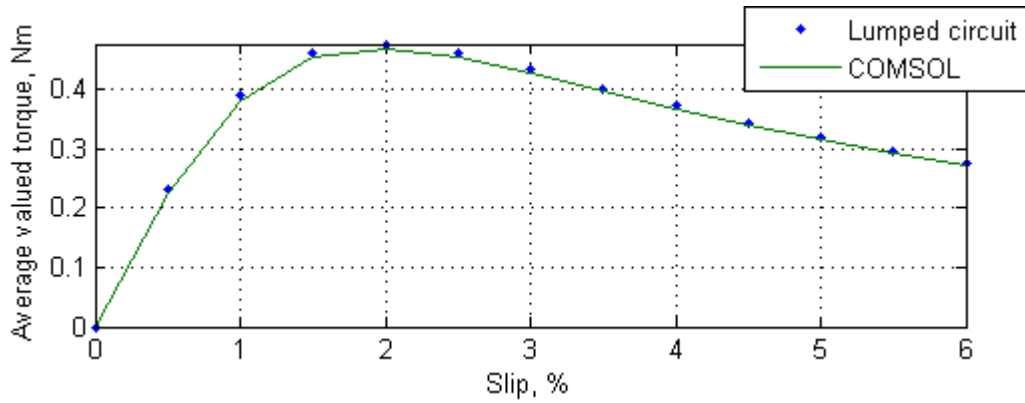


(b)

Figure 5-5 (a) Approximated curve of the phase inductance (absolute value) through data-points obtained in FEMM. (b) Average valued torque at 1A (peak) supply.



(a)

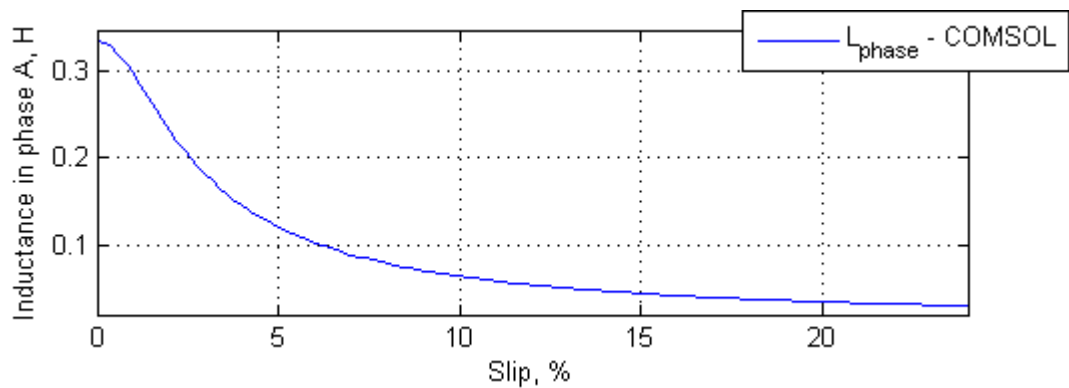


(b)

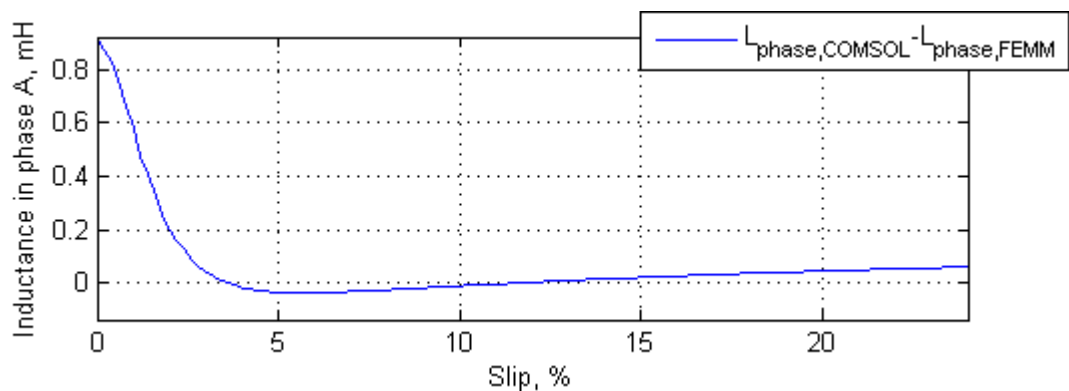
Figure 5-6 (a) Approximated curve of the phase Inductance (absolute value) through data-points obtained in COMSOL Multiphysics. (b) Simulated torque for 1A (peak) phase current.

5.6 COMPARISON BETWEEN SIMULATED PHASE INDUCTANCE AND TORQUE

Figure 5-7 (a) illustrates the phase inductance obtained in COMSOL Multiphysics. Figure 5-7 (b) shows that the difference in inductance between COMSOL Multiphysics and FEMM is highest at low slip. The difference is below 0.001H. There is a significant error-decrease as the slip is increased from 0% to $\approx 3.7\%$.



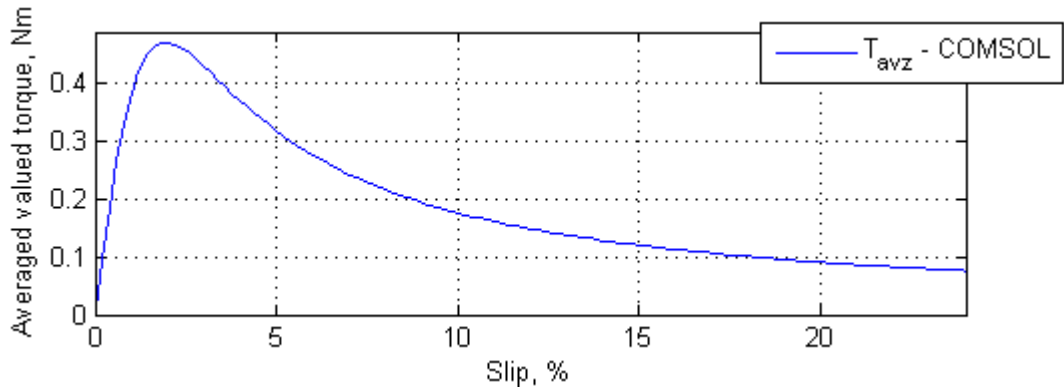
(a)



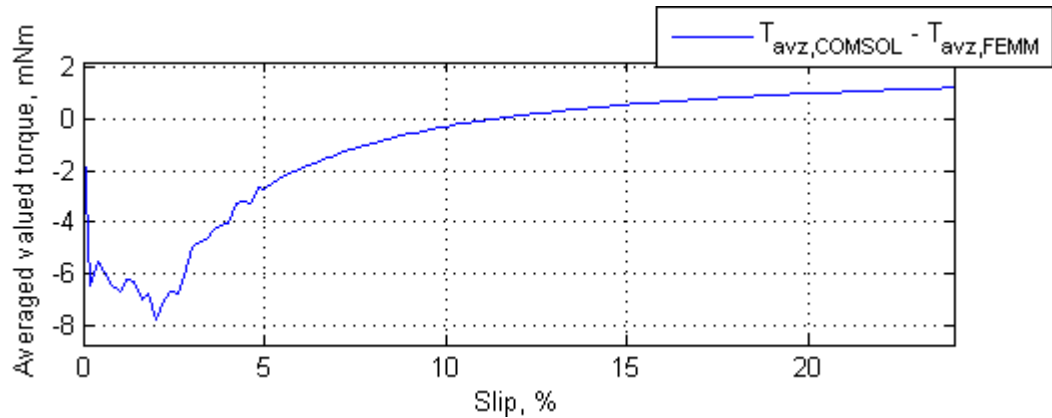
(b)

Figure 5-7 (a) Simulated phase inductance when the stator slots are supplied with 1A (peak) in COMSOL Multiphysics. (b) Difference in phase inductance between results obtained in COMSOL Multiphysics and FEMM.

Figure 5-8 (a) shows the simulated average valued torque in COMSOL Multiphysics. It is achieved by integrating over the force-domain as described in Section 2.11. Figure 5-8 (b) shows that the largest difference in torque between COMSOL Multiphysics and FEMM is 0.008Nm. The torque at the operating point (4.7% slip) is 0.33Nm in COMSOL Multiphysics. The corresponding value is 0.003Nm higher in FEMM. The difference between the torque in COMSOL Multiphysics and FEMM is highest at pull-out torque.



(a)



(b)

Figure 5-8 (a) Simulated torque in COMSOL Multiphysics for 1A (peak) stator supply. (b) Difference in simulated average valued torque between COMSOL Multiphysics and FEMM.

CHAPTER 6 TIME-DEPENDENT SIMULATION OF THE IM IN COMSOL

Results from the time-dependent simulations of the induction motor are presented in this chapter. The simulations are made in COMSOL Multiphysics at 4.7% slip. Time-dependent simulations cannot be made directly in FEMM in the time of writing this report. Calculations at the operating point of the IM are made in reference [20].

6.1 STATOR- AND ROTOR- CURRENT

Figure 6-1 shows two electric time periods of the three-phase stator currents supplied to the stator windings at 4.7% slip. The three phase system is defined as in *Section 2.3*. The motor is fed with 1A (peak).

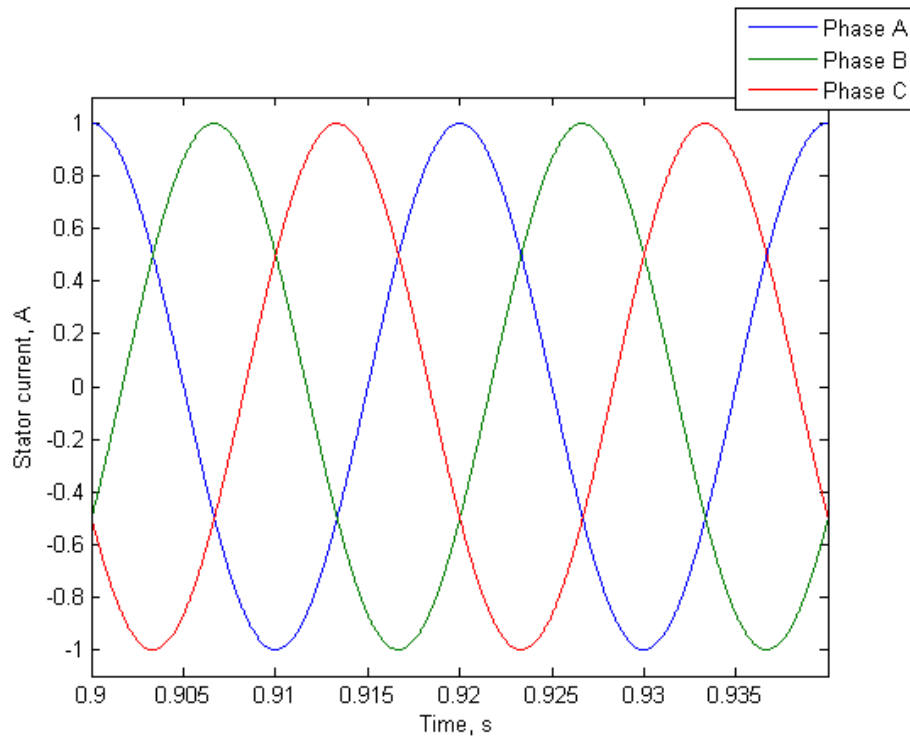
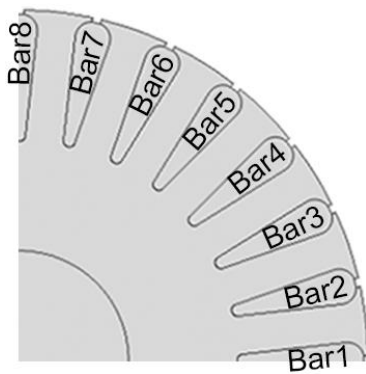
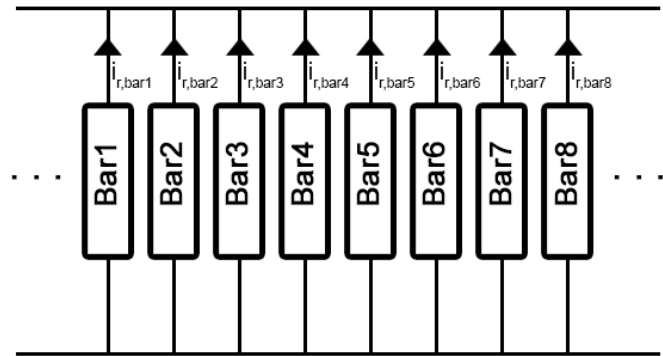


Figure 6-1 Stator current waveforms at 4.7% slip in COMSOL Multiphysics.

Figure 6-2 (a) and *(b)* show where the rotor bars are located and how they are coupled. *Figure 6-3* illustrates eight of the twenty-eight rotor bar currents at the operating point. The rotor time period is 0.45s. The currents are shifted in time as the bar number increases.



(a)



(b)

Figure 6-2 (a) Numbering of the rotor bars in one pole of the 2D cross-section of the induction motor. (b) Electric circuit of the rotor bars coupled in parallel.

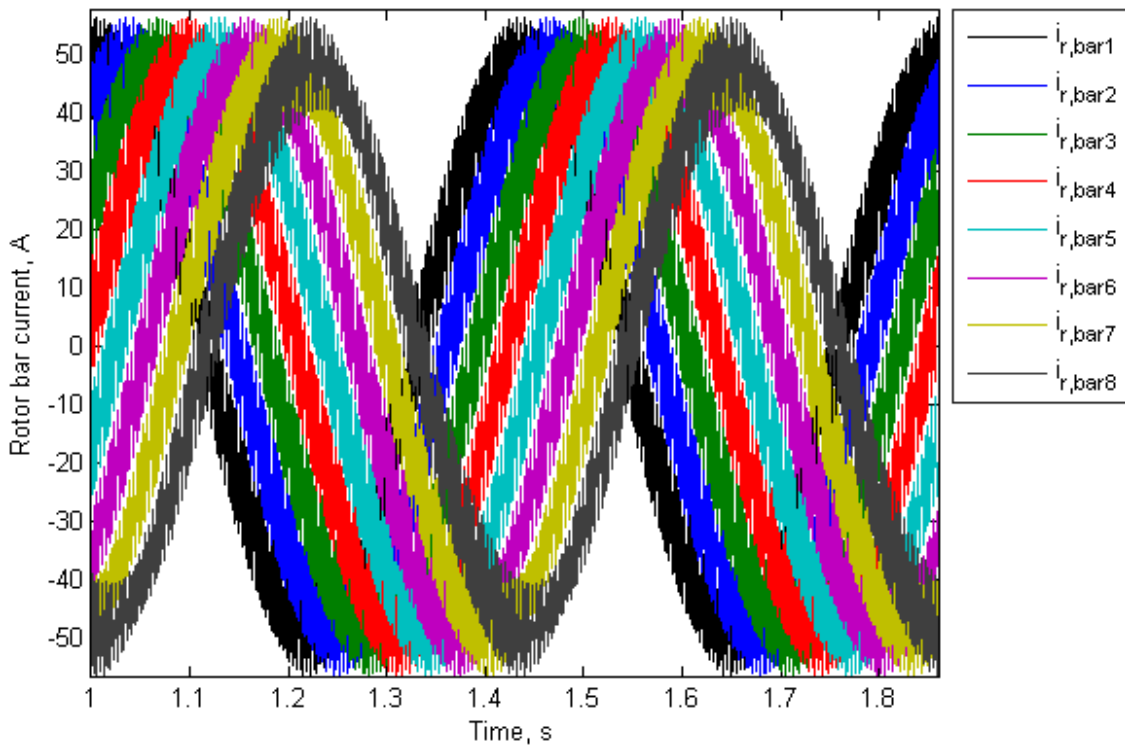


Figure 6-3 Eight rotor bar currents in COMSOL Multiphysics at 4.7% slip.

6.2 STATOR FLUX LINKAGE AND STATOR PHASE VOLTAGE

Figure 6-4 shows the stator phase flux linkage obtained by integrating the magnetic vector potential in the stator slots using *Equation 2-10*. The stator flux linkage is distorted. The harmonics that appear are present in the induced voltage as well.

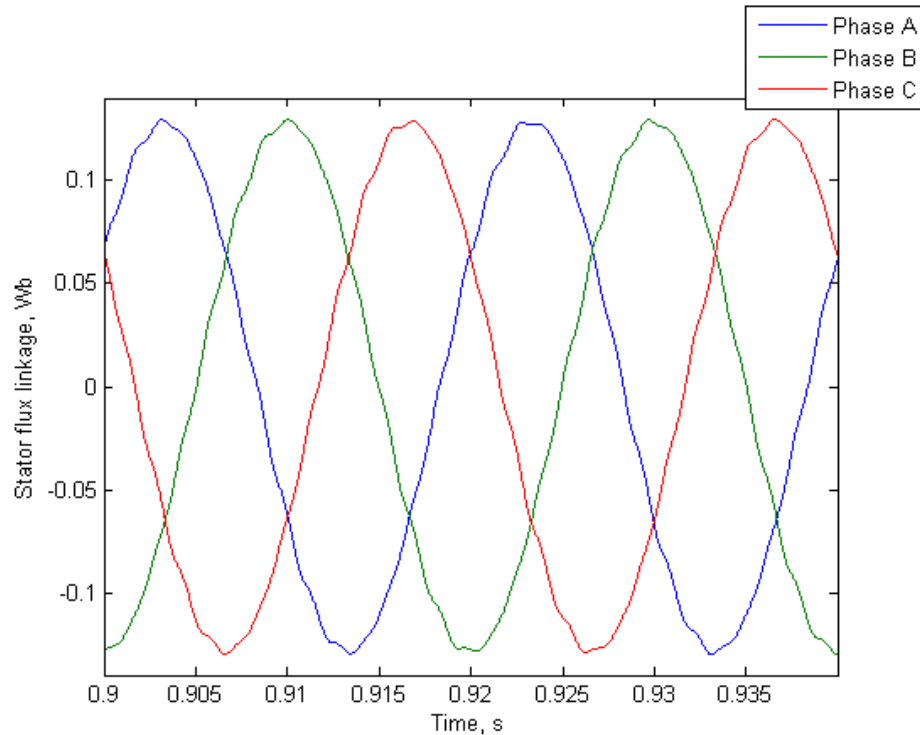
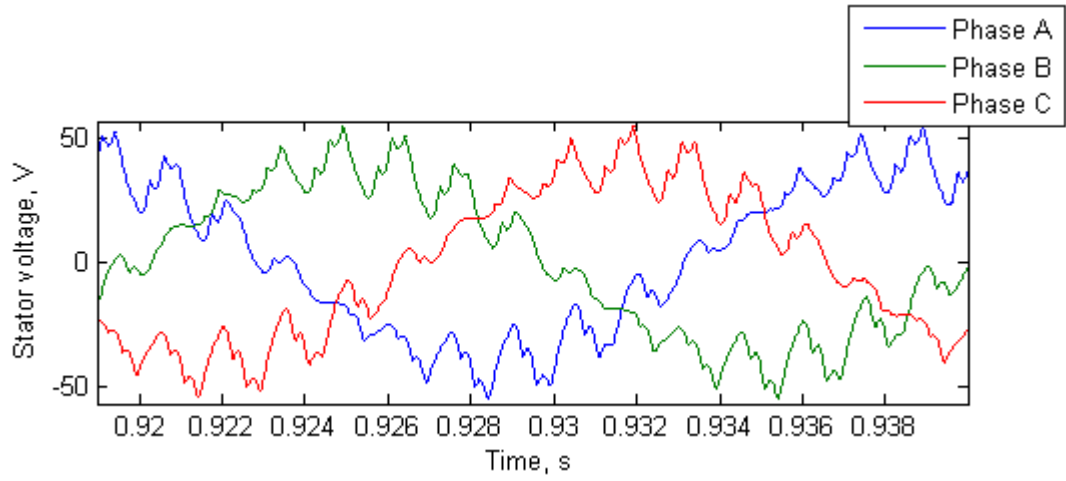


Figure 6-4 Stator flux linkage of the motor at 4.7% slip in COMSOL Multiphysics.

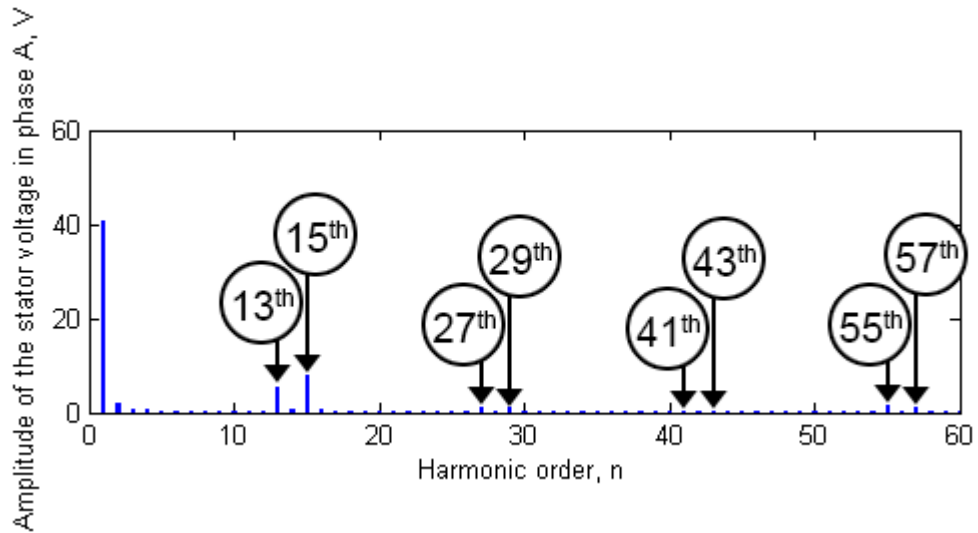
The waveforms of the induced stator phase voltage are seen in *Figure 6-5 (a)*. These curves are received by taking the time-derivative of the stator flux linkage per phase in *Figure 6-4* according to *Equation 6-1*. The amplitude of the fundamental stator voltage in phase A is 40V as seen in the bar chart in *Figure 6-5 (b)*. The harmonics appear in pairs at $n = 13^{\text{th}}, 15^{\text{th}}, 27^{\text{th}}, 29^{\text{th}}, 41^{\text{th}}, 43^{\text{th}}, 55^{\text{th}}, 57^{\text{th}}$. Even-order harmonics are not present due to half-wave symmetry.

$$V_s = \frac{d\psi_s}{dt}$$

Equation 6-1



(a)

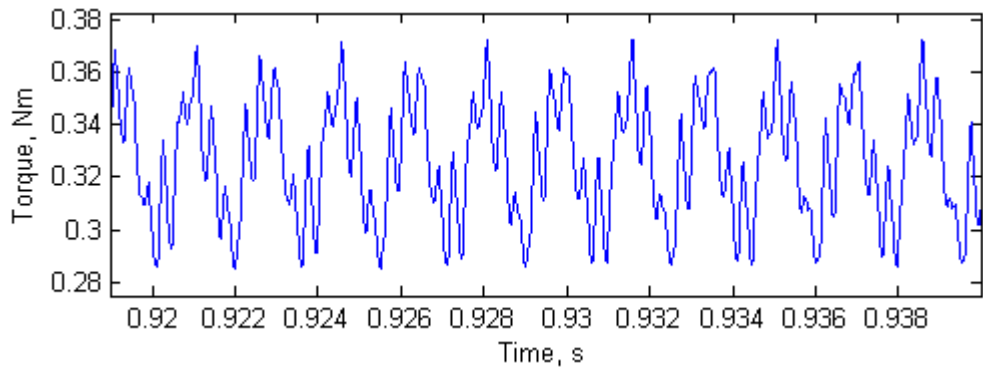


(b)

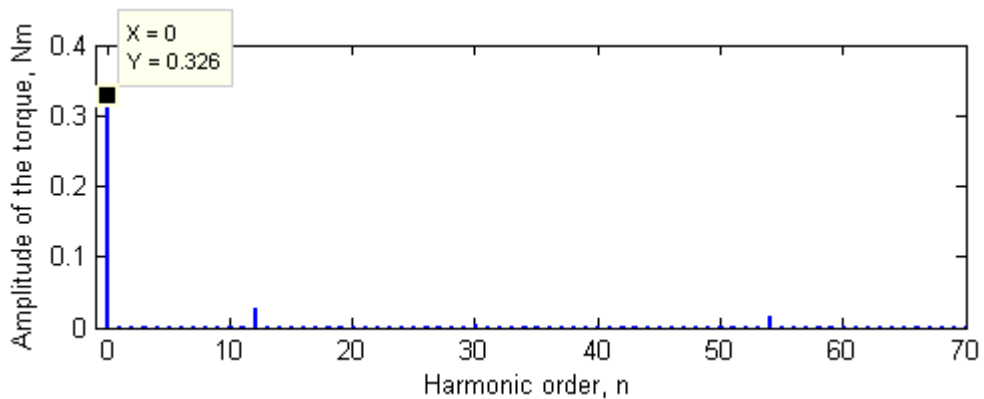
Figure 6-5 (a) Stator phase voltage and (b) amplitude spectrum of the voltage waveforms in phase A of the IM in COMSOL Multiphysics.

6.3 TORQUE AT 4.7% SLIP IN COMSOL MULTIPHYSICS

The torque at 1430rpm is seen in *Figure 6-6 (a)*. It is evaluated as described in *Section 2.11*. The DC-value is 0.33Nm as seen in *Figure 6-6 (b)*. The same value is received in the time-harmonic simulation in *Figure 5-8* at 4.7% slip. The harmonic orders 12th, 30th, 42th and 54th are present in the amplitude spectrum of the torque.



(a)

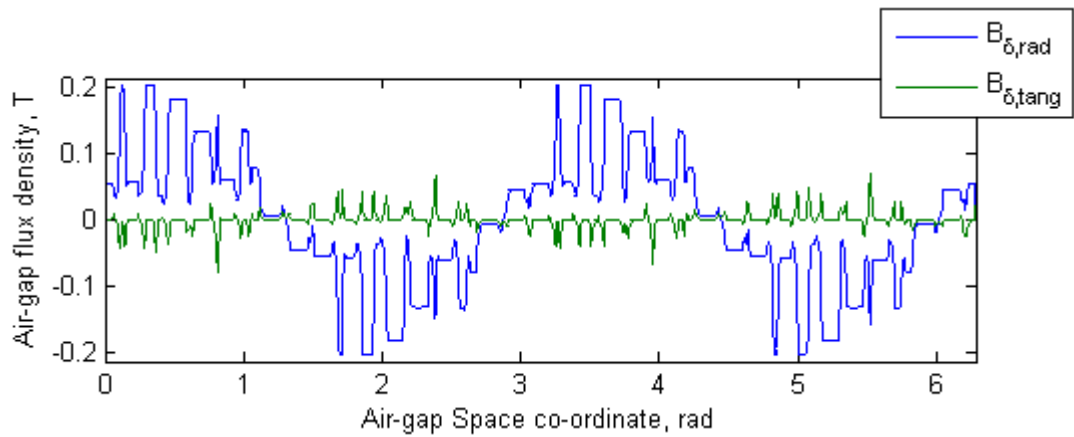


(b)

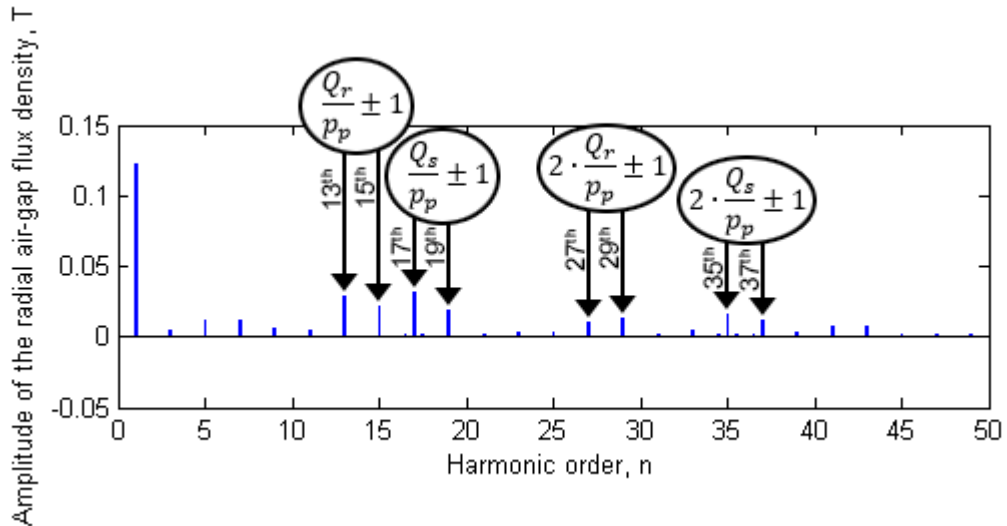
Figure 6-6 Torque at the operating point (1430rpm) and 1A (peak) supply as a function of time.

6.4 FLUX DENSITY ALONG THE MIDDLE OF THE AIR-GAP

Figure 6-7 (a) illustrates the spatial air-gap flux density along the middle of the air-gap over four poles at 4.7% slip. The harmonic spectrum of the radial air-gap flux density is seen in Figure 6-7 (b). The amplitude of the fundamental radial air-gap flux density is 0.12T. Rotor slot harmonics of order 13th, 15th, 27th and 29th are present. The harmonics of order 17th, 19th, 35th and 37th are stator slot harmonics. The expressions of the stator- and rotor- slot harmonics in Figure 6-7 (b) are based on reference [19].



(a)

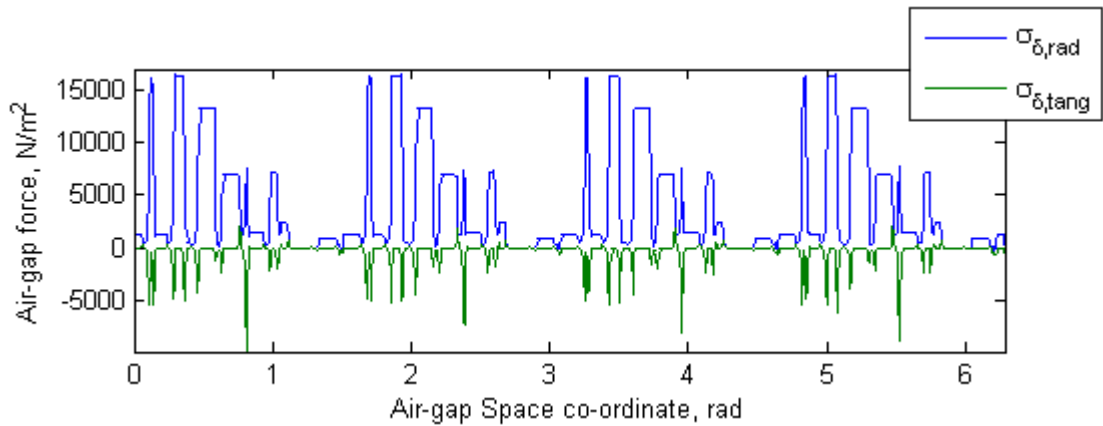


(b)

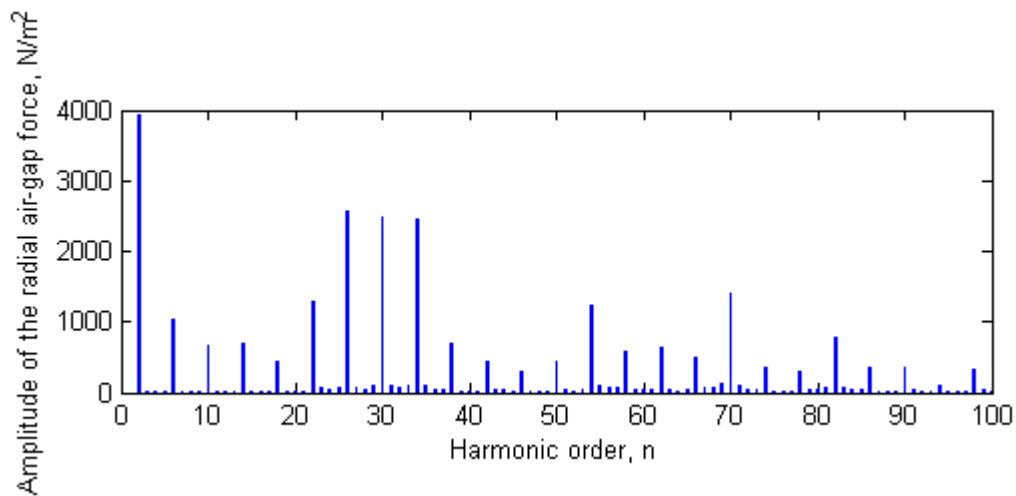
Figure 6-7 (a) Spatial air-gap flux density at the operating point, at time instant 2s. (b) Harmonic spectrum of the radial air-gap flux density.

6.5 AIR-GAP FORCE

The air-gap force at 4.7% slip in *Figure 6-8 (a)* is derived based on the radial- and tangential- part of the flux density along the air-gap in *Figure 6-7 (a)*. The equations of the force components are seen in *Section 2.11* (see *Equation 2-12* and *Equation 2-13*). The harmonic spectrum of the radial magnetic force is shown in *Figure 6-8 (b)*. The harmonic orders are located twice the orders of the radial flux density in *Figure 6-7 (b)*. The air-gap force can, as described in *Section 1.2*, be used to study motor vibrations.



(a)



(b)

Figure 6-8 (a) Air-gap force at the operating point, at time instant 2s, and 1A (peak) supply.
(b) Harmonic spectrum of the radial air-gap force.

CHAPTER 7 CONCLUSION AND FUTURE WORK

7.1 CONCLUSION

An electromagnetical COMSOL-model has been developed of a specific induction motor. The IM was supplied with 1A (peak) in the FEM-simulations. End-effects have been excluded. The time-harmonic simulations were validated with FEMM and an equivalent lumped model. The average-point value of the tangential flux density in the stator back was 0.63% higher in FEMM compared to COMSOL at no-load. The radial part of the magnetic flux density in the middle of the rotor tooth, at no-load, was 0.28% lower in FEMM compared to COMSOL. The difference of the absolute value of the radial air-gap flux density at no-load between COMSOL Multiphysics and FEMM was below 0.03T. The difference was below 0.02T for the tangential part. The maximum difference between the torque obtained in COMSOL Multiphysics and the torque derived based on the equivalent electric circuit was 0.009Nm. The deviation in stator flux linkage between COMSOL Multiphysics and FEMM was below 0.001Wb. The maximum difference between the torque obtained in COMSOL Multiphysics and FEMM was 0.008Nm. The torque at the operating point was 0.33Nm in the time-harmonic study in COMSOL. This value was also achieved in the time-dependent simulation at 4.7% slip. The corresponding value was 0.003Nm higher in the time-harmonic simulation in FEMM.

7.2 FUTURE WORK

The investigated induction motor was current supplied. The next step is to make a representative electromagnetical model of a voltage supplied motor in COMSOL Multiphysics. The starting point could be to make the model in 2D. End-effects could be accounted for by coupling external circuits to the field model, as seen in *Figure 7-1*. Additional circuits can be disregarded if the model is made in three-dimensions since end-effects are included in the field model. Motor vibrations could be studied in COMSOL Multiphysics based on the obtained radial magnetic forces.

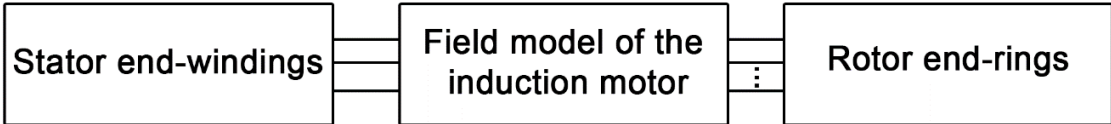


Figure 7-1 External circuits coupled to the field model to include the end-effects.

BIBLIOGRAPHY

The used references are gathered in the Bibliography.

- [1] K. C. Maliti, *Modelling and Analysis of Magnetic Noise in Squirrel-cage Induction Motors*. Stockholm, Sweden: Doctoral Dissertation, Department of Electric Power Engineering, Electrical Machines and Power Electronics, KTH, 2000.
- [2] S. L. Nau and H. G. G. Mello, "Acoustic noise in induction motors: causes and solutions," in *Petroleum and Chemical Industry Conference, 2000. Record of Conference Papers. Industry Applications Society 47th Annual, 2000*, pp. 253-263.
- [3] C. Sadarangani, *Electrical Machines – Design and Analysis of Induction and Permanent Magnet Motors*. Stockholm: Division of Electrical Machines and Power Electronics, KTH, 2006.
- [4] R. Haettel, "Problem description of Master thesis, Prediction of Magnetic Noise in a Traction Motor," ed. Västerås: ABB Corporate Research, 2013.
- [5] L. Kostetzer, F. Hetemi, and D. Gerling, "Scalable system simulation for electric drives," in *Electric Drives Production Conference (EDPC), 2011 1st International, 2011*, pp. 143-146.
- [6] M. Solveson, C. Rathod, M. Hebbes, G. Verma, and T. Sambharam, "Electromagnetic Force Coupling in Electric Machines," ed: ANSYS, inc., 2011.
- [7] F. Marion, "Magneto-vibroacoustic analysis: a new dedicated context inside Flux @11.2.," in *CEDRAT Magazine - N°65 - December 2013*, 65 ed, 2013.
- [8] F. Zidat, "Vibro-Acoustic Analysis for Noise Reduction of Electric machines," ed: CEDRAT, 2014.
- [9] R. Escarela-Perez, E. Melgoza, and E. Campero-Littlewood, "Time-Harmonic Modeling of Squirrel-Cage Induction Motors: A Circuit-Field Coupled Approach," in *COMSOL Conference, Boston, 2008*.
- [10] J. Güdelhöfer, R. Gottkehaskamp, and A. Hartmann, "Numerical Calculation of the Dynamic Behavior of Asynchronous Motors with COMSOL Multiphysics," in *COMSOL Conference Europe, Milan, 2012*.
- [11] J. F. Gieras, C. Wang, and J. C. Lai, *Noise of Polyphase Electric Motors*: Taylor & Francis, 2006.
- [12] S. Östlund, *Electric Railway Traction*. Stockholm: Electrical Machines and Power Electronics, 2011.
- [13] S. Östlund and M. Leksell, *EJ2200 Electrical Machines and Drives*. Stockholm: Electrical Machines and Power Electronics, 2010.
- [14] K. Delaere, R. Belmans, and K. Hameyer, "Influence of rotor slot wedges on stator currents and stator vibration spectrum of induction machines: a transient finite-element analysis," *Magnetics, IEEE Transactions on*, vol. 39, pp. 1492-1494, 2003.
- [15] S. I. Shahl. *Electrical Machines II, Lecture: Introduction to AC Machines*. Available: <http://uotechnology.edu.iq/dep-eee/lectures/3rd/Electrical/Machines%20II/Introduction.pdf>
- [16] M. Kaltenbacher, *Numerical Simulation of Mechatronic Sensors and Actuators* vol. 2nd Edition. Universität Erlangen, Germany: Springer - Verlag Berlin Heidelberg, 2007.

- [17] G. Engdahl, H. Edin, R. Eriksson, S. Hörnfeldt, and N. Schönborg, "Electrotechnical modeling and design," ed. Stockholm: Electromagnetic Engineering, KTH, 2011.
- [18] D. Meeker. (2009). *Finite Element Method Magnetics*. Available: <http://www.femm.info/Archives/doc/manual.pdf>
- [19] R. Chitroju, "Improved performance characteristics of induction machines with non-skewed symmetrical rotor slots," ed. Stockholm, Sweden: Licentiate Thesis, Electrical Machines and Power Electronics, School of Electrical Engineering, KTH, 2009.
- [20] D. Meeker. (2004). *Induction Motor Example*. Available: <http://www.femm.info/wiki/InductionMotorExample>
- [21] O. Wallmark. (2012). *EJ2210 Analysis of Electrical Machines, Task1: Analysis of an Induction Machine using a FEM Based Software*. Available: http://www.kth.se/polopoly_fs/1.299773!/Menu/general/column-content/attachment/EJ2210_fem_assignment.pdf
- [22] E. Holzbecher and H. Si, "Accuracy Tests for COMSOL - and Delaunay Meshes," in *COMSOL Conference*, Hannover, 2008.

LIST OF FIGURES

<i>Figures used in the report.</i>		<i>Page:</i>
<i>Figure 1-1</i>	<i>Coupling procedure for a vibro-acoustic analysis of an induction motor.</i>	<i>4</i>
<i>Figure 1-2</i>	<i>Indirect method for studying vibro-acoustics in Flux, [8].</i>	<i>4</i>
<i>Figure 2-1</i>	<i>Single-cage rotor with an: (a) open rotor bar, (b) closed rotor bar. (c) Double-cage rotor.....</i>	<i>9</i>
<i>Figure 2-2</i>	<i>(a) Three-phase winding arrangement over 2 poles (one pole pair). (b) Single layer winding, $q = 3$ slots per pole and phase.</i>	<i>10</i>
<i>Figure 2-3</i>	<i>(a) Y - and (b) Δ - connection of the voltage-fed stator winding.</i>	<i>11</i>
<i>Figure 2-4</i>	<i>(a) Magnetization curve. (b) Linear region of a BH-curve.</i>	<i>11</i>
<i>Figure 2-5</i>	<i>Distribution of the triangular mesh in a part of the air-gap.</i>	<i>12</i>
<i>Figure 2-6</i>	<i>Force-calculation surface and line.</i>	<i>14</i>
<i>Figure 3-1</i>	<i>Simplified equivalent circuit per phase of the induction motor at steady state.</i>	<i>15</i>
<i>Figure 4-1</i>	<i>(a) Cross-section of the induction motor with 4 poles, (b) smallest possible symmetry covering one pole-pitch of the motor.</i>	<i>18</i>
<i>Figure 4-2</i>	<i>Section of the: (a) coarse- and (b) refined- triangular air-gap mesh of the IM.</i>	<i>20</i>
<i>Figure 5-1</i>	<i>(a) Stator flux linkage per phase when the motor is supplied with 1A (peak). (b) Deviation in ψ_{sa} between COMSOL Multiphysics and FEMM.</i>	<i>21</i>
<i>Figure 5-2</i>	<i>Surface plot of the magnetic flux density (T) and contour lines of the magnetic vector potential (Nb/m) at no-load in (a) COMSOL Multiphysics, (b) FEMM.</i>	<i>22</i>
<i>Figure 5-3</i>	<i>(a) Radial component of the magnetic flux density at no-load. (b) Difference between results of the radial flux density in COMSOL Multiphysics and FEMM.</i>	<i>24</i>
<i>Figure 5-4</i>	<i>(a) Tangential component of the flux density at no-load. (b) Deviation in the tangential flux density between results obtained in COMSOL Multiphysics and FEMM.</i>	<i>25</i>
<i>Figure 5-5</i>	<i>(a) Approximated curve of the phase inductance (absolute value) through data-points obtained in FEMM. (b) Average valued torque at 1A (peak) supply.</i>	<i>26</i>
<i>Figure 5-6</i>	<i>(a) Approximated curve of the phase Inductance (absolute value) through data-points obtained in COMSOL Multiphysics. (b) Simulated torque for 1A (peak) phase current.....</i>	<i>27</i>
<i>Figure 5-7</i>	<i>(a) Simulated phase inductance when the stator slots are supplied with 1A (peak) in COMSOL Multiphysics. (b) Difference in phase inductance between results obtained in COMSOL Multiphysics and FEMM.....</i>	<i>28</i>
<i>Figure 5-8</i>	<i>(a) Simulated torque in COMSOL Multiphysics for 1A (peak) stator supply. (b) Difference in simulated average valued torque between COMSOL Multiphysics and FEMM.</i>	<i>29</i>
<i>Figure 6-1</i>	<i>Stator current waveforms at 4.7% slip in COMSOL Multiphysics.</i>	<i>30</i>
<i>Figure 6-2</i>	<i>(a) Numbering of the rotor bars in one pole of the 2D cross-section of the induction motor. (b) Electric circuit of the rotor bars coupled in parallel.</i>	<i>31</i>
<i>Figure 6-3</i>	<i>Eight rotor bar currents in COMSOL Multiphysics at 4.7% slip.....</i>	<i>31</i>
<i>Figure 6-4</i>	<i>Stator flux linkage of the motor at 4.7% slip in COMSOL Multiphysics.....</i>	<i>32</i>
<i>Figure 6-5</i>	<i>(a) Stator phase voltage and (b) amplitude spectrum of the voltage waveforms in phase A of the IM in COMSOL Multiphysics.</i>	<i>33</i>
<i>Figure 6-6</i>	<i>Torque at the operating point (1430rpm) and 1A (peak) supply as a function of time.....</i>	<i>34</i>
<i>Figure 6-7</i>	<i>(a) Spatial air-gap flux density at the operating point, at time instant 2s. (b) Harmonic spectrum of the radial air-gap flux density.</i>	<i>35</i>
<i>Figure 6-8</i>	<i>(a) Air-gap force at the operating point, at time instant 2s, and 1A (peak) supply. (b) Harmonic spectrum of the radial air-gap force.</i>	<i>36</i>
<i>Figure 7-1</i>	<i>External circuits coupled to the field model to include the end-effects.</i>	<i>37</i>



LIST OF TABLES

Tables used in the report.

	<i>Page:</i>
<i>Table 1-1 Main differences in references [9, 10].</i>	6
<i>Table 1-2 Main similarities in references [9, 10].</i>	6
<i>Table 1-3 Computer software-tools used in this thesis work.</i>	6
<i>Table 1-4 Simulation studies in this thesis work.</i>	7
<i>Table 4-1 Defined materials of the studied induction motor.</i>	19
<i>Table 4-2 Coarse- and refined- triangular mesh in the air-gap.</i>	20
<i>Table 5-1 Maximum value of the B-field at different regions at no-load operation (average value).</i>	23
<i>Table A-1 Data of the studied IM.</i>	I

APPENDIX

APPENDIX A SPECIFICATION OF THE INDUCTION MOTOR

Table A-1 *Data of the studied IM.*

Properties of Tutorial motor	Value
Number of poles:	4
Number of phases:	3
Number of stator slots:	36
Number of rotor bars:	28
Outer motor diameter:	130mm
Rotor diameter:	80mm
Air-gap thickness:	0.375mm
Active motor-length:	100mm
Number of turns per stator slot:	44
Stator fill factor:	0.397
Stator frequency:	50Hz (electric)
Operating point (Y-connected)	
Phase current:	1A (peak)
Speed:	1429.32rpm (4.7% slip)



APPENDIX B STATOR SLOT FILL FACTOR

The stator slot fill factor is defined in *Equation B-1*. The current density in the stator slots in COMSOL Multiphysics are displayed without dividing with the copper fill factor.

$$F_{fys} = \frac{A_{wire} \cdot N_t}{A_{ss}}, \quad \text{Equation B-1}$$

where F_{fys} is the stator slot fill factor, A_{wire} is the copper wire area.